5-2024

Computer Modeling of Normal Fault-Related Damage Zones: Implications for Estimating Geothermal Energy Potential

Audrey Jennings
Trinity University

Computer Modeling of Normal Fault-Related Damage Zones: Implications for Estimating Geothermal Energy Potential

Audrey Jennings

A DEPARTMENT HONORS THESIS SUBMITTED TO THE
DEPARTMENT OF GEOSCIENCES AT TRINITY UNIVERSITY
IN PARTIAL FULFILLMENT OF THE REQUIREMENTS FOR GRADUATION WITH
DEPARTMENTAL HONORS

DATE: April 12, 2024

Ben Surpless
THESIS ADVISOR (Ben Surpless)

Ben Surpless
DEPARTMENT CHAIR (Ben Surpless)

Jennifer Henderson, AVPAA

Student Agreement

I grant Trinity University (“Institution”), my academic department (“Department”), and the Texas Digital Library ("TDL") the non-exclusive rights to copy, display, perform, distribute and publish the content I submit to this repository (hereafter called "Work") and to make the Work available in any format in perpetuity as part of a TDL, digital preservation program, Institution or Department repository communication or distribution effort.

I understand that once the Work is submitted, a bibliographic citation to the Work can remain visible in perpetuity, even if the Work is updated or removed.

I understand that the Work's copyright owner(s) will continue to own copyright outside these non-exclusive granted rights.

I warrant that:

1) I am the copyright owner of the Work, or
2) I am one of the copyright owners and have permission from the other owners to submit the Work, or
3) My Institution or Department is the copyright owner and I have permission to submit the Work, or
4) Another party is the copyright owner and I have permission to submit the Work.

Based on this, I further warrant to my knowledge:

1) The Work does not infringe any copyright, patent, or trade secrets of any third party,
2) The Work does not contain any libelous matter, nor invade the privacy of any person or third party, and
3) That no right in the Work has been sold, mortgaged, or otherwise disposed of, and is free from all claims.

I agree to hold TDL, DPN, Institution, Department, and their agents harmless for any liability arising from any breach of the above warranties or any claim of intellectual property infringement arising from the exercise of these non-exclusive granted rights.”

I choose the following option for sharing my thesis (required):

[X] Open Access (full-text discoverable via search engines)
[ ] Restricted to campus viewing only (allow access only on the Trinity University campus via digitalcommons.trinity.edu)

I choose to append the following Creative Commons license (optional):

Table of Contents

List of Figures

List of Tables

Acknowledgements

Funding for this project was provided by 2022-2023 and 2023-2024 Keck Geology Consortium Advanced Research Project Grants as part of an NSF-REU Award to the Keck Geology Consortium (EAR 1659322; PIs Wirth, K., and Davidson, C.). Funding was also provided by NSF Award 2042114 to PI Benjamin Surpless and by funds provided by the Department of Geosciences, including the Tinker and Ed Roy Funds. Special thanks to Dr. Ben Surpless (for excellent advising and mentorship); to Audrey Davis and Rhea Kumar (for encouragement and baked goods); to Demi, Jack, Jasper, Michelle, Morgan, and Pierce (for lots of laughs); and to my family (for making all of this possible).

ABSTRACT

Geothermal energy is a growing clean energy resource, but the challenging identification of productive geothermal systems discourages significant utilization. However, previous research identifies normal fault zones as settings that can produce the fracture densities necessary for subsurface fluid flow and thus geothermal production. These areas of elevated deformation around faults, known as damage zones, can be useful proxies for geothermal potential, so understanding how damage zones develop under different conditions can be crucial for accelerating geothermal energy deployment.

To better understand geothermal potential in normal fault zones, I constructed 3D models in the Fault Response Modeling module of MOVE 2022 (by *Petex*). Each model consists of a single normal fault plane that extends to 5 km of depth at a dip angle of 70 degrees, intersecting surfaces consistent with the Navajo sandstone at 0.5 km, 2.0, and 3.0 km of depth. Models also approximate different fault zone conditions, including different amounts of vertical displacement and zero pore fluid pressure vs. realistic pore fluid pressure values. I also created model sets that approximate two different conceptual models of fault growth. In the Fault Propagation (FP) model, fault length and displacement accumulate at a relatively constant rate, and in the Constant Length (CL) model, the fault propagates rapidly to its final length early in its history, then displacement accumulates on that fixed-length fault. For all models, I documented maximum Coulomb shear stress (MCSS), maximum strain (E1), strain dilation, fracture orientation, and fracture intensity to approximate damage zone development.

Model results consistently predicted changes in the spatial distribution of damage zone development near fault centers, with high-intensity fracturing occurring proximal to the fault plane and stress and strain values increasing with greater fault displacements. At shallow depths

(0.5 km), models predict fault damage focused in the hanging wall, at moderate depths (2.0 km), the damage zone is symmetric about the fault plane, and at greater depths (3.5 km), the damage zone is focused in the footwall. I suggest that these changes in damage zone location are related to fault propagation direction, with upward propagation focused in the hanging wall and downward propagation focused in the footwall. However, damage zone distributions and predicted stress and strain values varied between fault propagation conceptual models (FP vs. CL), between models with different pore fluid pressures, and by depth within a given model. These results can be used by those targeting the high permeabilities associated with normal fault damage zones, especially in the western United States, where major normal faults and high heat flows coincide.

INTRODUCTION

In the 21st century, many nations have sought to diversify their energy resources to promote energy security, slow climate change impacts, and meet stated environmental goals (e.g., Boden, 2017). Geothermal energy is a prime candidate for energy diversification due to its status as a renewable energy resource and its ability to continually generate energy regardless of environmental conditions (e.g., Cross, 2009). However, to be productive at the utility-scale, geothermal energy systems require both high subsurface heat flow and connected fluid pathways.

The most common methods of utility-scale geothermal energy generation use steam to turn electricity-generating turbines (e.g., Boden, 2017). To produce this steam, efficient geothermal energy systems place fluids in the subsurface into contact with rocks heated by the Earth's natural geothermal gradient or nearby magmatism, then transfer these fluids to conduits where the fluid is flashed to steam. This rapid volume expansion spins turbines, which produces electricity (e.g., Sharmin et al., 2023). Due to the very specific natural conditions required for utility-scale geothermal electricity production, companies have found it challenging to locate suitable geologic targets; the financial risks associated with mis-identifying geothermal settings have largely deterred wide-scale geothermal energy research and investment in recent years (e.g., Micale et al., 2014; Chelminski, 2022). Therefore, developing new methods for identifying promising geothermal settings will be crucial to finally utilizing this energy resource at a large scale.

Fault zones are known to be conducive to geothermal energy production (e.g., Faulds and Hinds, 2015). These locations concentrate the intense stress and strain associated with fault slip and lead to the development of intense fracturing proximal to faulting. Regions of elevated fault-related deformation are called damage zones and have been widely investigated as potential

settings for geothermal energy production due to their elevated permeability (e.g., Micale et al., 2014; Faulds and Hinz, 2015; Shervais et al., 2024); nearly all geothermal systems rely on subsurface fractures for efficient production (e.g., Grant and Bixley, 2011). In a survey of geothermal systems throughout the Basin and Range province, where heat flow values are especially high (Fig. 1), Faulds and Hinz (2015) identified a range of normal fault zone geometries that are especially conducive to geothermal fluid upwelling, largely based on their structurally controlled subsurface fracture permeability. Thus, further investigating damage zone formation in normal fault zones is a crucial step in expanding geothermal energy production in the United States.

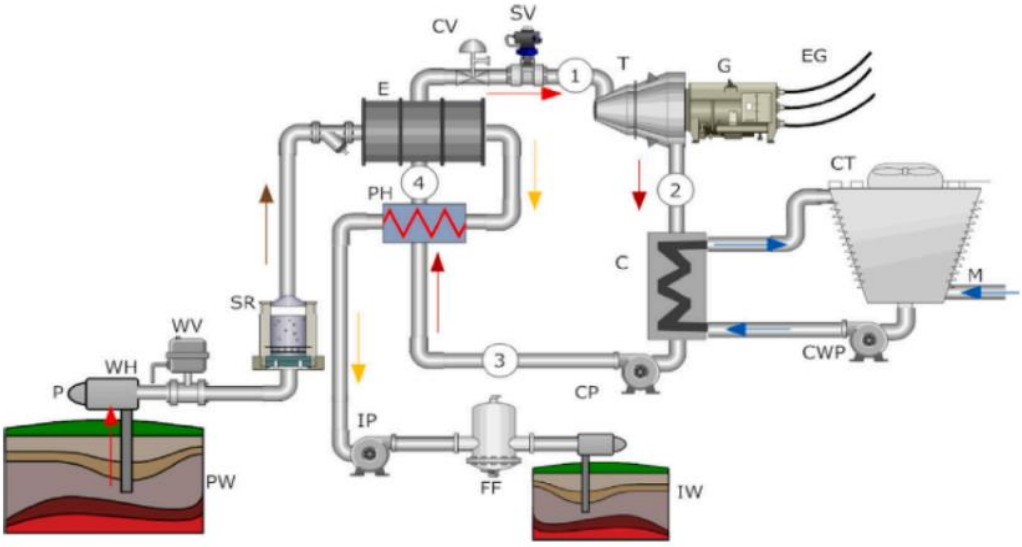

PW	Production well	E	Evaporator	CV	Control valve
P	Pump	PH	Preheater	SV	Stop valve
WH	Wellhead	IP	Injection pump	T	Turbine
WV	Well valve	FF	Final filter	G	Generator
SR	Sand remover	IW	Injection well	EG	Electric grid
C	Condenser	CP	Condensate pump	CWP	Cooling water pump
M	Make-up water	CT	Cooling tower		

Figure 1. Schematic diagram of a binary geothermal power plant (Sharmin et al., 2023).

However, field-based geothermal exploration is expensive and may not always lead to the successful identification of geothermal development sites (e.g., Micale et al., 2014; Shervais et al., 2024). Thus, lower-cost exploration options like 3D computer modeling of fault and fracture

networks are an effective way to investigate damage zones and associated subsurface fluid flow. Software like *Move* 2022 (by Petex) enables users to model faults and predict variables like stress, strain, fracture intensity, and fracture orientations from user-designed geologic models, providing insight into fault-related deformation in damage zones and thus into geothermal development potential in different geologic settings. In this study, I use 3D computer modeling to assess the influence of different geologic variables (including fault displacement, fault propagation, and pore fluid pressure) on damage zone development in a simple normal fault system. Through this work, I aim to answer a range of research questions, including:

1. How do stress, strain, and fracturing evolve within a propagating fault system over time, and how do different fault propagation models impact the evolution of stress and deformation?
2. What effects do fault-related stress and strain fields have on fracturing orientations and intensities within the rock volume?
3. How does the distribution of fault-related fracturing vary with depth and accumulated displacement?
4. Can we use 3D modeling results to aid in the identification of locations with especially high permeability and thus geothermal potential?

To address these questions, I constructed 3D models of normal faults in *Move 2022* (by Petex), generated stress, strain, and fracture predictions for each, and compared these results to field studies to assess the ability of these models to predict damage. With these models, I can compare the impacts of accumulated slip, depth, and how different conceptual models of fault propagation affect the development of stress and strain patterns within a fault system. By analyzing these results in the context of collected field data and previous damage zone studies, I

propose a new strategy that uses 3D modeling as an additional predictive tool that can be used in conjunction with more traditional methods of geothermal exploration.

BACKGROUND

Geothermal Energy Production

As fluids flow through subsurface regions with a high geothermal gradient, they become heated and can be used to produce large quantities of steam, which can be used to drive electric turbines, thus fulfilling the same role as fluids heated by coal or natural gas in a typical electric plant (e.g., Sharmin et al., 2023) (Fig. 1). While subsurface heat flow is a critical component of geothermal energy production, this process also depends on a highly permeable rock volume that allows fluids to contact hot rock and turn into steam (e.g., Speer et al, 2014; Sharmin et al., 2023; Shervais et al., 2024). Thus, production sites for geothermal energy development must provide both elevated heat flows and high permeabilities, which can be difficult to find without expensive subsurface exploration. While heat flow across much of the United States and world has been mapped (Fig. 2), subsurface regions with the level of fluid flow connectivity required to

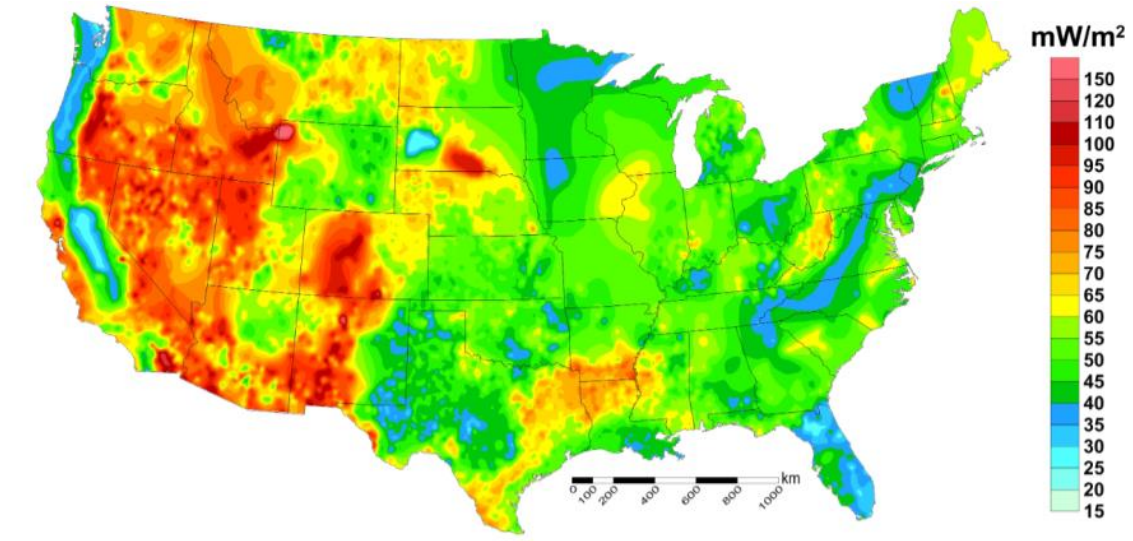

Figure 2. Map of estimated heat flow across the conterminous United States (Blackwell et al., 2011).

support geothermal systems are often harder to identify (e.g., Speer et al, 2014; Houwers et al., 2015; Shervais et al., 2024). Traditional strategies for permeability identification and geothermal exploration may include drilling into the subsurface to look for the presence of heated, mobile fluids, or using seismic data to pinpoint regions with underground pockets of fluids (e.g., Boden, 2017). Such strategies can be effective but typically either require massive upfront financial investment, or struggle to locate specific locations for development (e.g., Micale et al., 2014).

One way to make geothermal energy viable in regions where only permeability OR heat flow are optimal (or where these values are unknown) is by developing different types of geothermal infrastructure targeted towards specific energy needs (e.g., Sharmin et al., 2024). Largely, this development has focused on harnessing different levels of heat flow. Systems with heat flow under 100 degrees typically cannot generate enough steam for electricity generation but may be used for directly heating fluids or buildings. Systems between 100 and 175 degrees C also fail to create large quantities of steam from typical geothermal fluids, which has led to the development of binary geothermal systems (e.g., Andrews and Jelley, 2022). Such systems pass fluids with very low boiling points through a “heat exchanger” that uses these low-boiling-point fluids to super-heat geothermal fluids beyond what would otherwise be possible, creating steam and generating electricity similarly to a classic flash system (e.g., Andrews and Jelley, 2022; Sharmin et al., 2023) (Fig. 1).

Despite the numerous ways that engineers have solved temperature constraints in geothermal energy generation, each system still relies on consistent permeability to function. A typical geothermal system requires an average fluid flow rate of 200 kg/s, as well as a fracture permeability of local material between 0.05 and 0.5 darcies (1 darcy = volumetric flow rate of 1 cm^3/s of water with a viscosity of 1 centipoise over a cross-sectional area of $1cm^2$ under a

pressure gradient of 1 atmosphere per centimeter), to maintain levels of fluid flow necessary for useful energy production (e.g., Boden, 2017). Due to the importance of consistent fluid flow in geothermal production, identifying settings with high-level permeability in these productive ranges will be key to establishing utility-scale geothermal energy generation.

Geologic Settings of High-Potential Geothermal Systems

Faulds and Hinz (2015) highlighted eight distinct geologic settings that hold especially high potential for geothermal energy development. These include major normal fault segments, fault bends, horsetail fault terminations, breached step-overs or relay ramps, fault intersections, accommodation zones between fault dip domains, displacement transfer zones along strike-slip fault zones, and transtensional pull-aparts (Fig. 3). Notably, most of these geometries occur

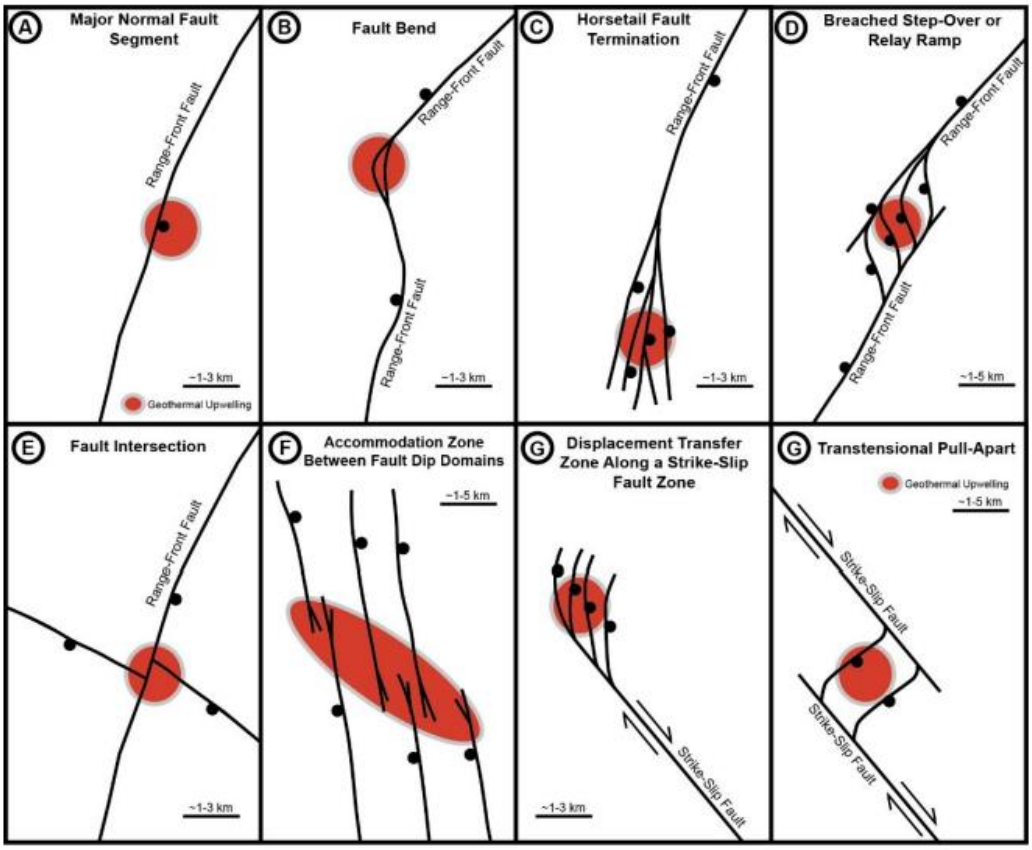

Figure 3. Locations of geologic settings most associated with geothermal energy potential in the Basin and Range province (Faulds and Hinz, 2015).

within extensional geologic settings (Faulds and Hinz, 2015), indicating that normal-fault-associated deformation enhances subsurface fluid flow. The displacement of rock volumes along a normal fault plane in an extensional setting generates zones of elevated stress and strain. These high-stress, high-strain environments produce regions of intense deformation known as damage zones, and they also form other geologic structures, like relay ramps, which promote high levels of subsurface fluid flow (Fig. 3).

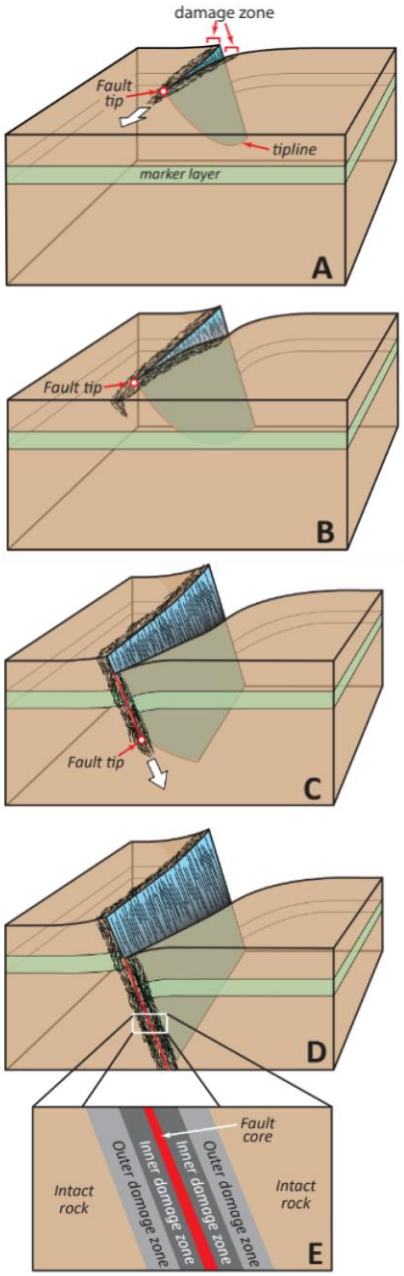

Figure 4. **Damage zone architecture and evolution**. Damage zone development with continuing fault propagation (A – D) and expected damage zone architecture around the propagating fault plane (E). Modified from Fossen (2016) and Liao et al. (2020).

Damage zones commonly consist of zones of deformation that decrease in intensity with distance from the fault (e.g., Berg and Skar, 2005; Savage and Brodsky, 2011; Choi et al., 2016). The greatest intensity of fracture and shear-related deformation occurs in the fault core, with inner and outer damage zones that display decreasing intensities of fracturing with distance from the fault plane, until fracturing no longer affects the intact rock involved in faulting (Fig. 4) (e.g., Liao et al., 2020). Damage zones may form asymmetrically, with the width and intensity of deformed regions differing between the hanging wall (HW) and footwall (FW) (e.g., Berg and Skar, 2005; Choi et al., 2016; Liao et al., 2020). In some studies of normal faults, the hanging wall displays greater extents of deformation relative to the footwall

(Fig. 4) though relative asymmetries vary by fault (e.g., Berg and Skar, 2005; Liao et al., 2020). Deformation can also vary by structural position along a fault, with three typical damage zone locations (e.g., Kim et al., 2004), including along the wall of the fault (damage along the central portion of the fault plane), the tip of the fault (concentrated deformation at the edges of the fault plane), and where two faults link (damage associated with interactions between different fault segments) (Fig. 5). Because stress conditions vary by structural position within a fault system, damage zones develop differently at different locations within a fault zone. Because of the reliance of geothermal energy potential upon fluid flow in damage zones (e.g., Faulds and Hinz, 2015), it is crucial to better understand the evolution of damage zone development more efficiently target subsequent field-based geothermal exploration t within normal fault zones to.

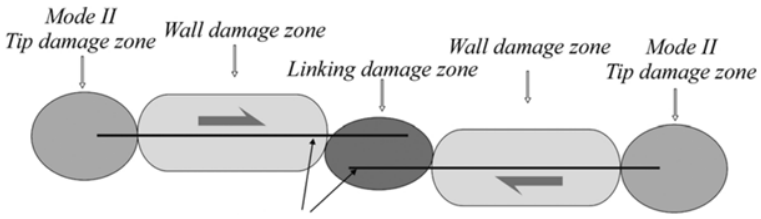

Figure 5. Types of damage zone. Locations of tip, wall, and linking damage zones within a multi-segment fault zone. Linking damage zones are represented in dark grey; wall damage zones are represented in light gray; and tip damage zones are represented in medium gray. Modified from Kim et al. (2004).

Fault Propagation

As faults propagate and accumulate displacement over time, the generated stress field varies, potentially leading to different patterns of damage zone formation at different times in a fault's history (e.g., Rotevatn et al., 2019). However, how faults propagate laterally and accumulate displacement during that propagation is not entirely understood. Ideas about fault-growth fall into two distinct conceptual models: the fault propagation model (FP) (e.g., Cartwright et al., 1995; Cowie et al., 2000; Kim and Sanderson, 2005) and the constant length model (CL) (e.g., Cowie, 1998; Walsh et al., 2002; Nicol, 2005; Jackson et al., 2017) (Fig. 6). The fault propagation model posits that a fault lengthens horizontally as it accumulates vertical

displacement, such that the fault is growing horizontally and vertically at roughly the same proportional rates (e.g., Cowie et al., 2000; Kim and Sanderson, 2005; Rotevatn et al., 2019). In contrast, the constant length model describes fault growth as a process of rapid accumulation of horizontal length when the fault forms and then remains at a relatively constant length as the system accumulates dip-slip displacement (e.g., Cowie, 1998; Nicol, 2005; Rotevatn et al., 2019). However, neither conceptual model has emerged as a more accepted model of fault growth (Rotevatn et al., 2019). Because fault propagation and associated displacement accumulation are the most significant sources of stress, strain, and fracturing within normal fault systems, better understanding the implications of *both* models for the evolution of stress, strain, and fracture development is critical for evaluating damage zones associated with faults at locations with high geothermal potential.

METHODS

Model Construction

To investigate damage zone development in normal fault zones, I utilized the Fault Response Modeling (FRM) module of Move 2022 (by Petex). This module calculates 72 distinct geologic variables based on user-designed 3D fault scenarios. Users can control the shape of a fault, the number of fault segments involved, the lithology of layers experiencing faulting, the type of fault movement, and a wide range of other model specifications. Because the FRM module permits users to model a wide array of fault geometries and styles of fault

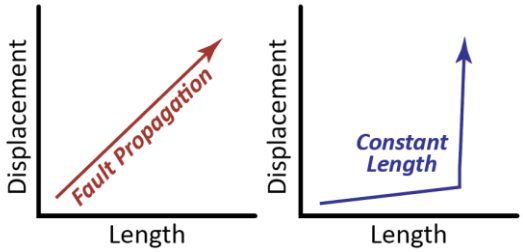

Figure 6. **Conceptual fault growth models**. Displacement vs. length relationships for the Fault Propagation (red) and Constant Length (blue) models of fault growth (Nicol et al., 2005).

movement, I was able to evaluate the effects of different geologic variables on model-dependent outputs like stress, strain, fault throw, fracture intensity, and fracture orientation. Thus, the FRM module permits me to analyze variations in patterns of damage zone development related to changing conditions.

The FRM module utilizes boundary element modeling (BEM), in which the program calculates specified variables at defined observation points across the model, rather than performing calculations at every possible location within the model (Petex, 2020). These calculations are based on the movement and flexure of blocks of material relative to the fault plane. Models constructed with the FRM module cannot incorporate frictional tractions acting along the fault plane. However, even without considering friction, performing calculations for every point within a large-scale model would require extremely high computing power and generate unwieldy quantities of data, making a boundary element approach practical for modeling fault zones at the kilometer scale (e.g., Crider and Pollard, 1998; Cooke, *unpub*.).

I specified a 20 m x 40 m sampling grid on the model observation surfaces, such that the software calculates values once per every 20 m x 40 m area on the observation surface, taking the spacing into account. This sampling density allows for meter-scale observations within the computing capabilities of my present resources. I constructed three different sets of fault models within the FRM module, calculating the resulting values for variables of interest (maximum Coulomb shear stress, E1 (strain value in the orientation of maximum strain), and strain dilation (increase in volume related to rock deformation)) at the meter scale across 3 different depths (0.5 km, 2 km, and 3 km). Each model also consists of a single, 5 km-long fault segment dipping at 70 degrees from the horizontal (Fig. 7; Table 1).

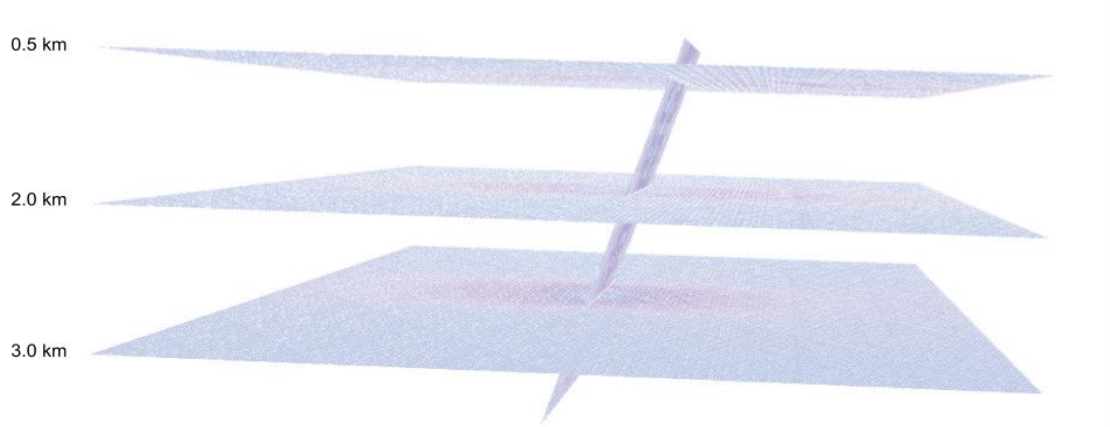

Figure 7. Fault model geometry in sideview. The topmost observation layer is located at 0.5 km-depth beneath the surface; the middle observation layer is located at 2.0 km-depth; and the bottommost layer is located at 3.0 km-depth.

In my models, fault slip is distributed in an elliptical shape, with the focus of slip occurring near the center of the plane in map view, and at 750 m below the top of the fault (Table 2). This aligns with previous modeling by Crider and Pollard (1998) which utilized an elliptical model of fault slip to approximate realistic distributions of slip (Fig. 8). The use of elliptical fault surfaces incorporates the highest displacements near the fault center that gradually decrease with distance, ultimately reaching 0 m displacement at the fault tips. This concept, known as slip tapering (Fig. 8), has been widely observed in field studies (e.g., Crider and Pollard, 1998).

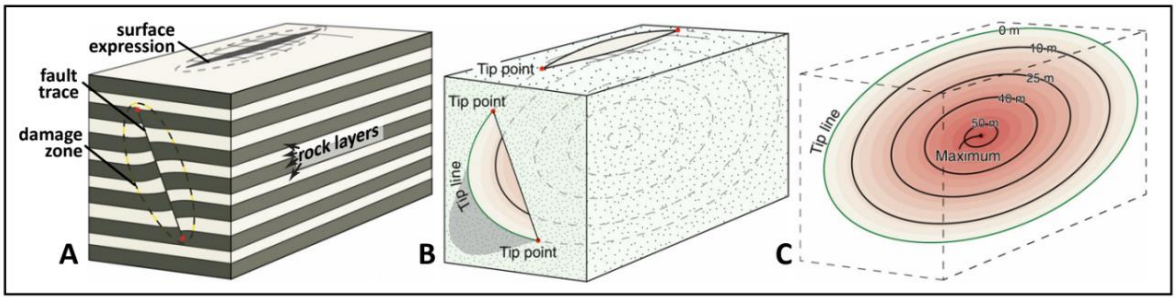

Figure 8. Elliptical fault plane framework. Maximum fault slip occurs near the midpoint of the fault plane (centroid) at depth and decreases to 0 m at the fault tips. Modified from Fossen (2016).

I also set every observation surface to mimic the lithological properties of the Navajo sandstone, which has elastic moduli with a Young's modulus value of 3.0 x 10^5 Pa (axial stress applied per axial strain) and a Poisson's ratio of 0.25 (strain perpendicular to the applied load per strain parallel to the applied load) (Schultz, 2010). To further simulate the Navajo sandstone, I established a coefficient of friction of 0.40, an internal friction angle of 30 degrees, a cohesion value of 2.00 MPa, and a material density of 2,495 kg/m^3 (Table 3). The Navajo sandstone is present throughout a wide area across the Basin and Range province (e.g., Fossen et al., 2011), a promising region for geothermal development due to its history of extension and resultant faulting and high heat flow (e.g., Faulds and Hinz, 2015). Thus, by defining the properties of our observation surfaces to be like those of the Navajo Sandstone, I can better apply the model results to real world geothermal potential.

Because Mohr circle analysis helps scientists visualize a local stress field and resulting fracture formation (e.g., Ferrill et al., 2011), we can use this to consider whether a given lithology, like the Navajo Sandstone, will fracture, based on the Mohr-Coulomb failure envelope for that material in a given stress field (Fig. 9). On this type of diagram, which displays normal versus shear stress values field, one can plot maximum (σ_1) and minimum (σ_3) principal normal stresses to construct the Mohr circle. In the case of a normal fault system, the maximum stress is vertical (applied by gravity acting on the overlying rock column) and the minimum stress is horizontal (Fig. 9). The Mohr circle represents all possible normal and shear stresses associated with that stress field, with the maximum shear stress value (MCSS) at the top or bottom of the circle. The failure envelope, which is determined experimentally, represents values at which fracture would occur in an intact rock. The higher the MCSS value, the more likely that fracture

will occur. However, even if the circle does not intersect the failure envelope, pre-existing weaknesses in the rock or microfractures may permit fractures to form.

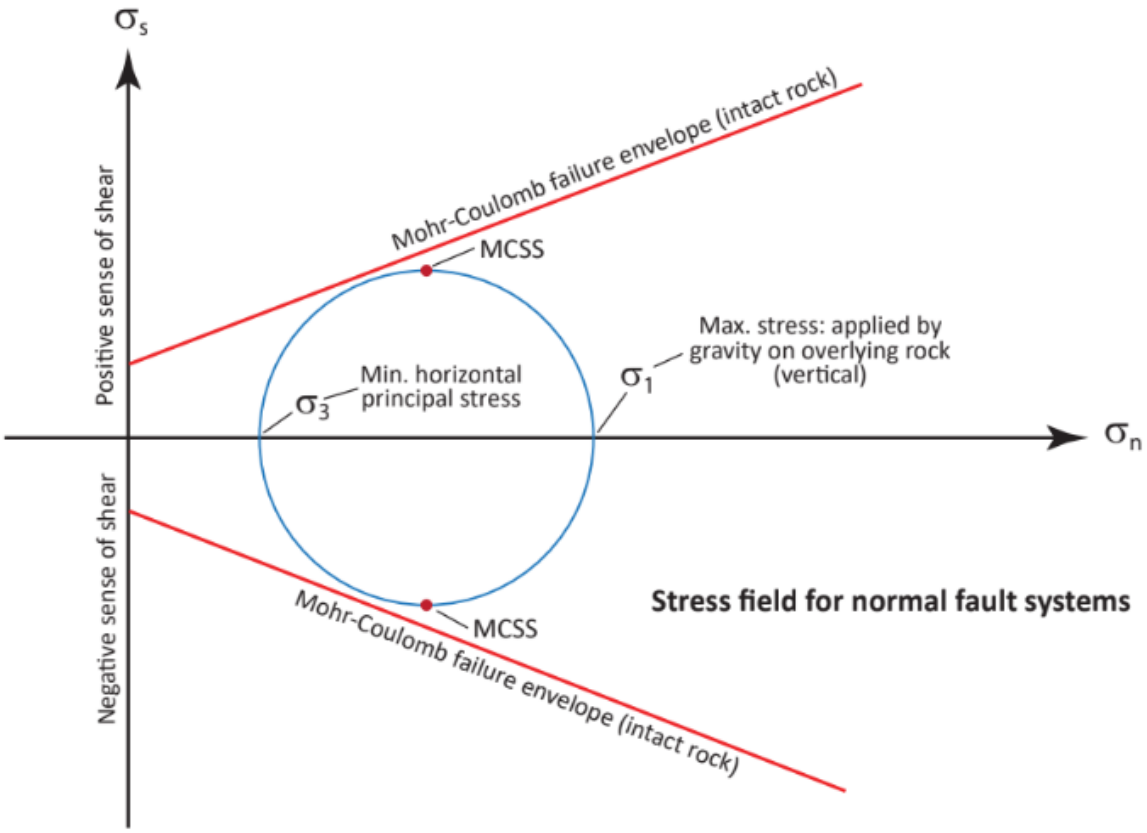

Figure 9. **Mohr circle diagram**. The Mohr Circle (blue) is drawn from shear stress values (y-axis) and normal stress values (x-axis) of the observed stress field. The Mohr-Coulomb failure envelope (red) describes shear stress and normal stress relationships that represent failure of previously intact rock. If the Mohr Circle intersects the Mohr-Coulomb failure envelope, intact rock will fail. Significantly modified from Fossen (2016).

I defined the pore fluid pressures for each observation surface by depth in each model, with pore fluid pressures of 5.2 MPa for the 0.5 km-depth surface, 20.6 MPa for the 2 km-depth surface, and 36.0 MPa for the 3 km-depth surface of every model. These values are based on hydrostatic pressure calculations using water density, acceleration due to gravity, and the depth of each observation surface, such that input pore fluid pressure mimics possible pore fluid pressures in a real-world system. I also built a model with a pore fluid pressure value of 0 MPa for each observation surface depth, creating a control model to compare stress, strain, and

fracturing results. This allows me to gauge the impact of pore fluid pressure on damage zone development in normal fault systems that may have high geothermal potential.

To model the potential impacts of the fault propagation (FP) model on damage zone development (Fig. 6), I constructed three different normal fault segment models which mimic a simultaneous increase in vertical displacement and lateral increase in fault length (Table 4). The first model represents the early stages of fault development, with a short fault segment (3 km long) experiencing low displacement (10 m). The second model, mimicking the middle stages of fault development, consists of a 4.5 km long fault segment experiencing 50 m of slip. I simulated the final stages of fault development (FP theory) with a 6 km fault segment undergoing 200 m of vertical displacement. To simulate fault development according to the constant length (CL) propagation model, I kept the fault segment at 6 km of length across all three models and gradually increased the vertical displacement in the same manner as the FP models: first 10 m of slip, then 50 m, and finally 200 m (Table 2, Fig. 10).

For each set of models, I recorded maximum Coulomb shear stress (MCSS), E1 (principal strain), and strain dilation. Because increasing shear stress values increase the likelihood of rock failure, the spatial distribution of high MCSS values represents the rock volume where fracturing is most likely. E1 represents strain in the principal strain direction such that greater E1 values represent greater extensional strain related to the normal faulting. Since stress generates deformation as strain, we can use high MCSS and E1 values as a proxy for deformation within damage zones. Strain dilation is also a useful proxy for damage zones and geothermal potential because it represents a measure of potential increase in open space within a rock, like permeability.

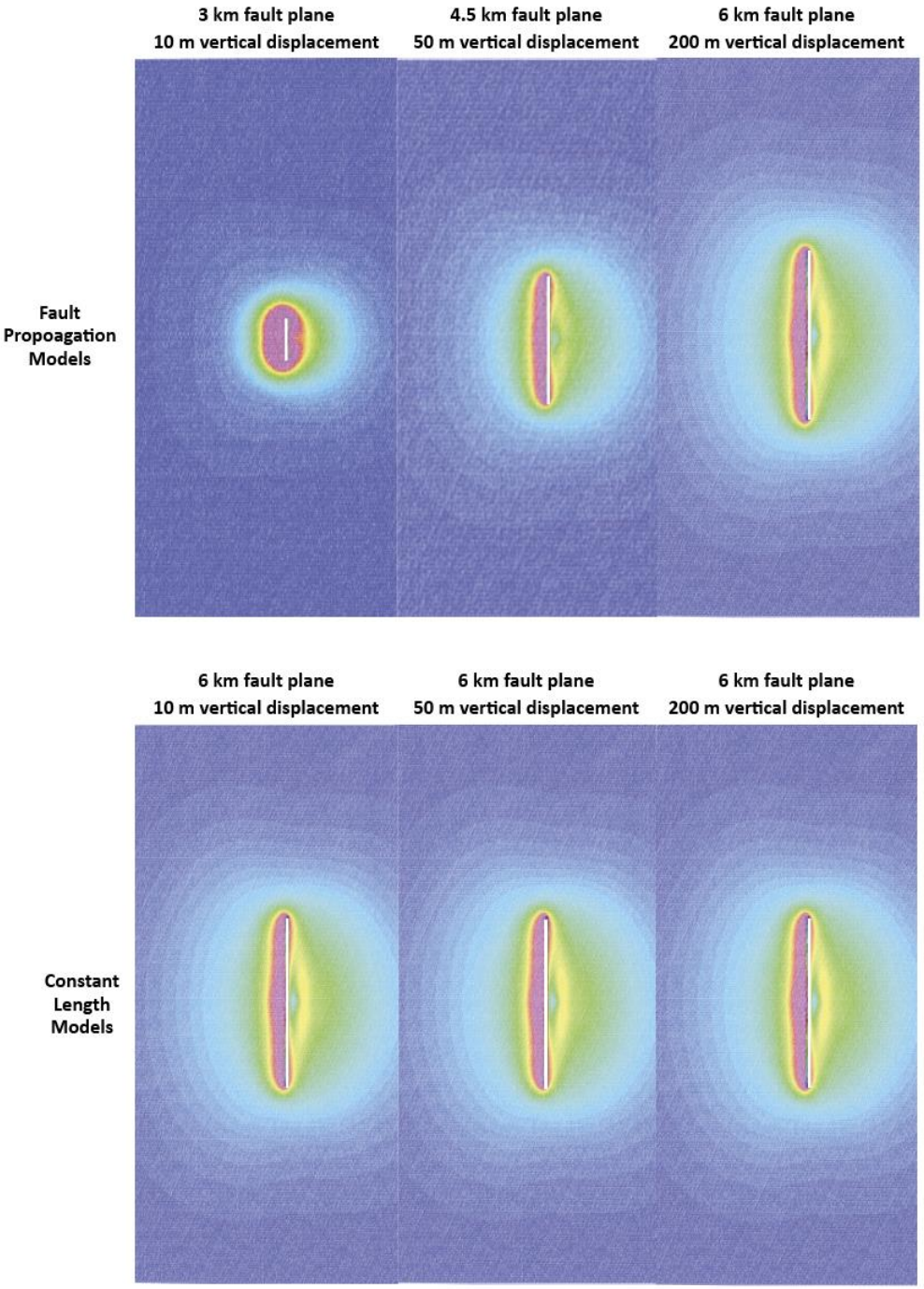

Figure 10. **Fault Propagation and Constant Length fault growth models**. Constructed models simulating the Fault Propagation (top) and Constant Length (bottom) theories of fault growth. Models are shown from the top, with fault lengths represented by white lines. The hanging wall lies to the left of each fault plane, and the footwall lies on the right. Fault models are overlain MCSS predictions for a 6 km fault plane (shown at 0.5km of depth) experiencing 200 m of displacement, approximating the CL End model. Warmer values indicate greater MCSS values.

Table 1. Fault Plane Characteristics

PROMPT	INPUT
STRIKE (IN MAP VIEW)	180 degrees
DIP ANGLE	69.94 degrees
TOP OF FAULT	0.0 km
BOTTOM OF FAULT	-5.0 km

Table 2. Fault Slip Distribution Specifications

PROMPT	INPUT
U1	3,000 m
U2	3,000 m
V1	6,000 m
V2	6,000 m
ORIENTATION	90 degrees
CENTROID	0, 0, -750.0 m

Table 3. Navajo Sandstone Characteristics

PROMPT	INPUT
POISSON'S RATIO	0.25
YOUNG'S MODULUS	30,000 MPa
COEFFICIENT OF FRICTION	0.40
FRICTION ANGLE	30 degrees
COHESION	2.00 MPa
DENSITY	2,495 kg/m^3

Table 4. Conceptual Fault Model Specifications

MODEL	FAULT SEGMENT LENGTH	VERTICAL DISPLACEMENT
CONSTANT LENGTH (START)	6 km	10 m
CONSTANT LENGTH (MIDDLE)	6 km	50 m
CONSTANT LENGTH (END)	6 km	200 m
FAULT PROPAGATION (START)	3 km	10 m
FAULT PROPAGATION (MIDDLE)	4.5 km	50 m
FAULT PROPAGATION (END)	6 km	200 m

The FRM module also predicts fracture orientation and intensity across a given model. BEM-model-generated fracture orientations predict how fractures would form if failure occurred at a given location relative to the fault, and fracture intensity describes how concentrated fracturing is at that point. Since fracture orientations impact flow direction in the subsurface, and high fracture intensity signifies high geothermal energy potential, modeling these variables for every model is crucial for gaining a comprehensive insight into how geothermal energy potential varies relative to a steeply dipping normal fault, including how models of fault evolution, depth, and pore fluid pressure influence them.

When running models in the FRM module, variables can be shown both visually (through heat maps overlain on the observation surfaces) and numerically (through the calculations of variables performed at every observation point). To gather visual data, I saved images of each heat-mapped observation surface with associated scale bars for each variable. I also saved the fracture intensity and fracture orientation visualizations for each model run (overlain on the associated E1 heat map); larger dots represent more intense fracturing, and the orientation of a generated rectangle indicates the predicted fracture orientation. For the numerical data, the FRM module provides a spreadsheet of the values for each variable calculated at every sampling point in the model. I trimmed this data to include just my variables of interest (MCSS, E1, and strain dilation) before exporting it to Excel. Once in Excel, I further narrowed the dataset to only include variables at specific points spaced regularly across the fault system, such that they generate cross-fault profiles of each variable from the fault center to the fault tips (Fig. 11). This collection of points allows us to observe how variables change both parallel to strike (from center to tip), as well as strike-perpendicular (from the hanging wall to the footwall). With this

parsed dataset, I then graphed MCSS, E1, and dilation across each defined profile of the fault plane to visualize damage zone evolution within a single fault model, as well as between different types of fault models.

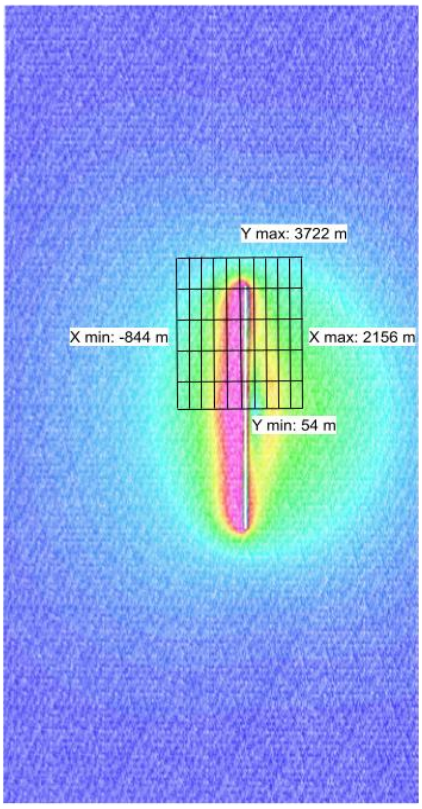

Figure 11. Sampling distribution. Sampling grid for my model data collection, approximated in black. MCSS, E1, and strain dilation values at each intersection of the grid were collected from the modeling output calculations and exported to Excel for further graphical analysis. Sampling grid overlies the MCSS heatmap for a 6 km fault plane experiencing 200 m of vertical displacement at 0.5 km of depth; warmer colors indicate greater MCSS values.

DATA AND RESULTS

After running all model sets and saving all generated heatmaps, I produced 18 graphs per fault geometry model. This includes 6 graphs per observation surface for a given fault geometry model, leading to a total of 108 graphs overall. By analyzing the graphed datasets produced by increasing amounts of vertical displacement at constant fault length (for the CL models) and by increasing amounts of vertical displacement and lateral growth (for the FP models), I can compare how variables change spatially around the fault plane in general, as well as how they change as fault growth continues in each model of fault evolution. For each fault model, I also investigated the relationship between depth in a normal fault system and damage zone development by comparing the graphed variable datasets for each observation surface in a single model. Finally, I compared the graphed datasets of a model with pore-fluid pressure (PFP) values of 0 MPa (for observation surfaces at 0.5 km, 2.0 km, and 3.0 km depth) to the same model with realistic PFP values, allowing me to analyze the potential impacts of pore fluid pressure on damage zone

development. For all comparisons, analyses are also supported by the generated heat maps that visualize variables of interest across the model.

Model Similarities

There were several trends in variable values that did not change with depth, magnitude of vertical displacement, lateral growth, model of fault propagation, or pore fluid pressure values. For example, in every scenario, the MCSS and E1 variables closely mimicked each other, as observed by comparing the MCSS and E1 heatmaps for the CL End model (Fig. 12). The changes in these values relative to the fault plane are nearly identical, indicating that MCSS and E1 values change in an identical manner within a given model. For every type of model tested, I also observed a consistent trend in the locations of E1 and MCSS maximum and minimum values. Near the fault center, the predicted variable values are greater than for the same variable at the fault tips, regardless of the perpendicular distance of the sampling point from the fault plane.

The observed similarities between MCSS and E1 distribution for a given model are expected. Stress creates strain, making it reasonable to expect high E1 values occurring as a response to high MCSS in the same area. The locations of these regions, representing damage zones, also seem reasonable given the parameters of my models. To mimic fault-slip tapering in real-world normal fault systems, the models experience their maximum vertical displacement at the fault center. This vertical displacement decreases from the fault center towards the tip, such that the fault tips of the models experience 0 m vertical displacement. By concentrating vertical displacement at the fault center, stress becomes elevated in this region relative to the rest of the system, leading to the higher stress and strain values near the central portion of the fault plane in all models.

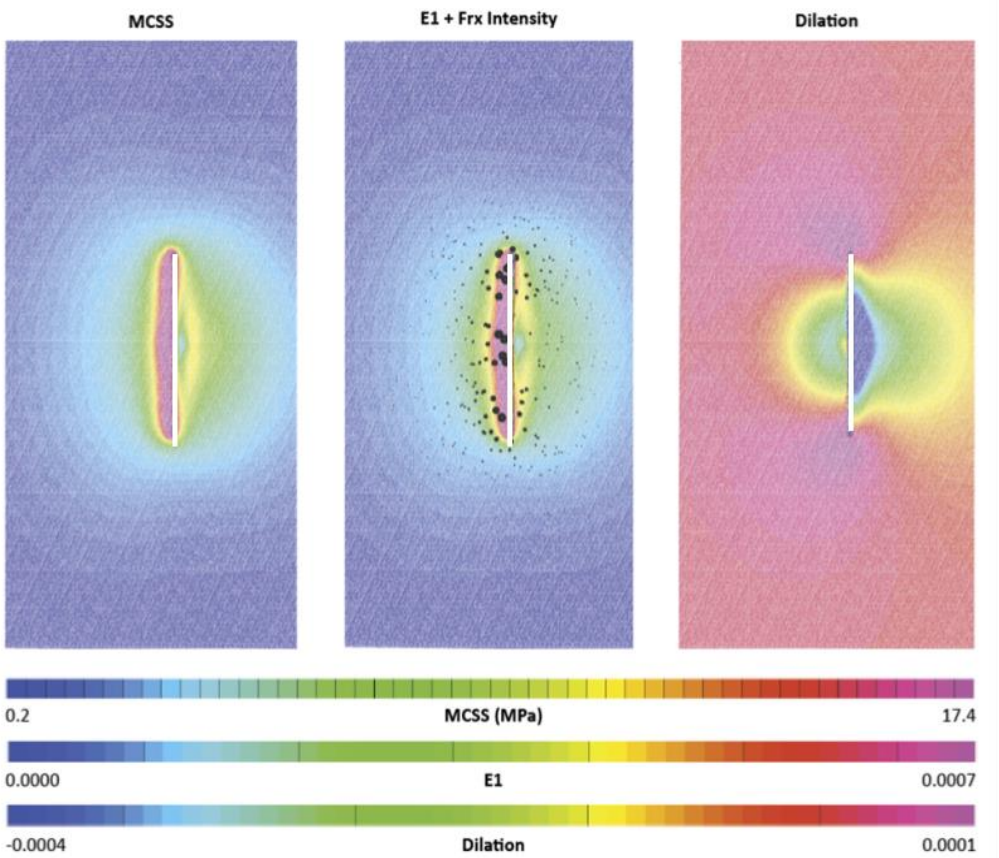

Figure 12. **Distribution of damage zones**. Predicted MCSS (left), E1 (middle), and dilation (right) values for the 0.5 km depth surface of a model experiencing 200 meters of vertical displacement along a 6 km fault plane. This model represents the Constant Length model with realistic pore fluid pressures included. Warmer colors represent higher values; cooler colors represent lower values. Fracture intensity is also depicted on the E1 surface, with larger black dots representing greater fracture intensity at a given point.

However, these areas do not always also show high dilation values, as described below, indicating that considering MCSS and E1 in isolation do not necessarily permit accurate prediction of the spatial distribution of high dilation zones within a fault system. For every observation surface in each model, the FRM module also produced spatial distributions of fracture orientation and intensity. Fracture orientations are represented on heat maps as planes generated in the orientation of fractures (if they were to form at that point). Fracture intensity is represented as dots, with larger dots signifying more intense fracturing in each area.

Across all model and observation surfaces, fracture intensity was greatest in regions of high MCSS, high E1, and/or dilation (Fig. 13). In all models, fractures predicted near the fault tips point towards the ends of the fault plane. However, fracture orientations near the fault center vary with depth and vary between the hanging wall and the footwall. In the top observation surface (0.5-km depth), fractures near the fault center are generally parallel to the fault plane in the hanging wall and perpendicular to the fault plane in the footwall (Fig. 14). However, the bottom observation surfaces (3.0-km depth) show the reverse (fractures near the fault center are perpendicular to the fault plane in the hanging wall and parallel to the fault plane in the footwall). The location of damage zones relative to the fault also changes with depth in the system, indicating that the changing fracture orientations may be related to where high-intensity damage zones occur.

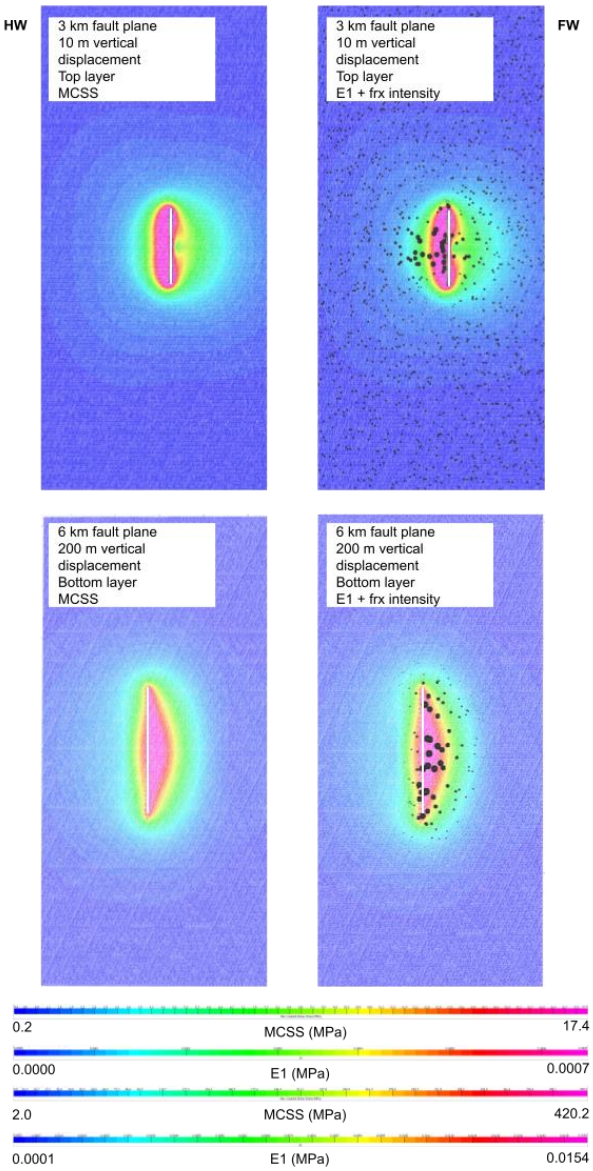

Figure 13. **Fracture intensities**. Predicted MCSS (left) and E1(right). Top row of heatmaps shows (at 0.5 km of depth) a 3 km fault plane experiencing 10 m of displacement, approximating the FP Start Model. Bottom row of heatmaps shows (at 3.0 km of depth) a 6 km fault plane experiencing 200 m of displacement, approximating the FP Start Model. Warmer colors represent higher values; cooler colors represent lower values. Fracture intensity is also depicted on the E1 surface, with larger black dots representing greater fracture intensity at a given point.

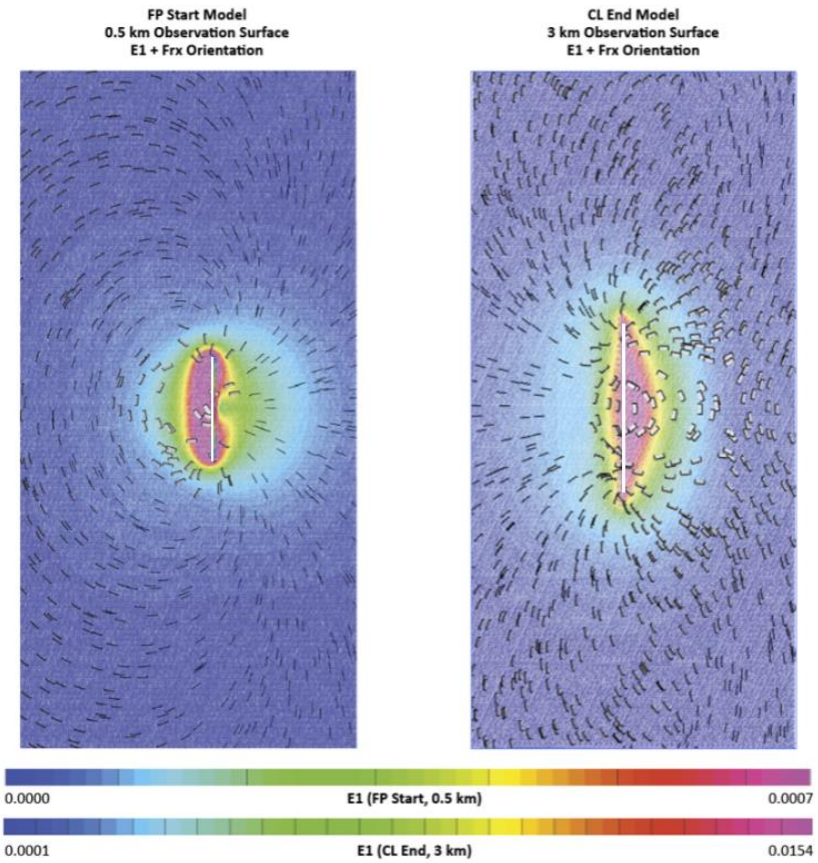

Figure 14. **Fracture orientations**. Left: predicted fracture orientations layered over predicted E1 values for the 0.5 km depth surface of a model experiencing 10 meters of vertical displacement along a 3 km fault plane. This model represents the start of the Fault Propagation model with realistic pore fluid pressures included. Right: predicted fracture orientations layered over predicted E1 values for the 3 km depth surface of a model experiencing 200 meters of vertical displacement along a 6 km fault plane. This model represents the end of the Constant Length model with realistic pore fluid pressures included. Warmer colors represent higher values; cooler colors represent lower values. Fracture orientations are depicted as rectangular planes in line with the predicted orientation of fracture formation at a given point, if fracturing was to occur.

Fault Displacement

I used the same set of fault displacements (10, 50, and 200 meters) for all models. In all models, greater fault displacement is associated with proportionally higher predictions of MCSS, E1, and dilation values. Additionally, the locations of high variable values within a model remain in the same position relative to the fault plane across all vertical displacements. For example, the MCSS colormaps of the CL model experiencing 10 m of vertical displacement and 200 m of vertical displacement appear almost identical (Fig. 15). However, the 200 m model predicted

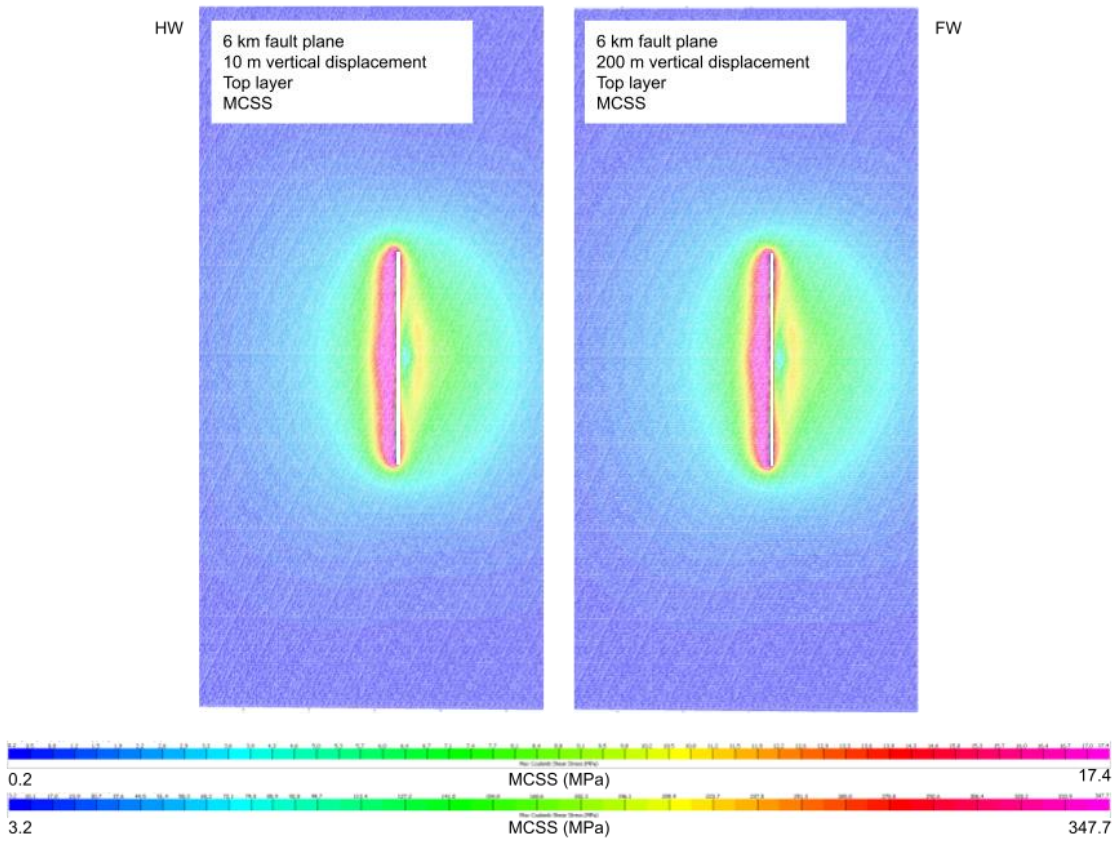

Figure 15. **Fault displacement**. Predicted MCSS for the 0.5 km depth surface of a 6 km fault plane experiencing 10 m of fault displacement, representing the CL start model (left), and predicted MCSS for the 0.5 km surface depth of a 6 km fault plane experiencing 200 m of fault displacement, representing the CL end model (right). Both models include realistic pore fluid pressures. Warmer colors represent higher values; cooler colors represent lower values.

MCSS values between 3.2 and 347.7, about 10 times greater than the 4.24 to 34.34 range predicted by the 10 m model.

The positive relationship between high stress and strain values and increased vertical displacement is evident in each fault propagation model and for all pore fluid pressures tested, as well as for each depth of observation surface. Such a relationship indicates that the amount of vertical displacement is a dominant influence on the levels of stress and deformation in normal fault zones, regardless of other co-influencing factors, and thus is important for establishing damage zones. However, the observation that the *locations* of damage zones within a given model do not change with displacement magnitude indicates that their extent is decided by

factors other than displacement. Possibly, initial fault displacement sets the extent of damage zones early in the history of a fault, and continued displacement manifests as increased stress and deformation in already weakened zones, rather than as new deformation in intact rock.

Depth

Depth in each fault model also impacts the spatial distribution of damage zone development, with the location of greatest damage shifting across the fault plane from the top (0.5 km depth) surface to the bottom (3 km depth) surface. For all PFP values and fault propagation models, the top observation surfaces predict most regions of high E1 and MCSS within the hanging wall and lower values within the footwall, but as depth increases, the maximum values shift towards fault plane in the hanging wall at the middle depth surface (2.0 km), and shift to the footwall at 3.0 km depth (Fig. 16). Though locations of high predicted strain dilation do not always correlate with high MCSS and/or high E1 areas in our models, strain dilation does appear to also vary in location with depth (as do MCSS and E1). Whether high strain dilation occurs primarily near the fault center or the fault tips appears to be largely controlled by the depth, with high dilation values concentrated at fault tips at near-surface depths (Fig. 12). Regions of high E1, high MCSS, and high dilation occur adjacent to the fault plane in all models and at all depths, however.

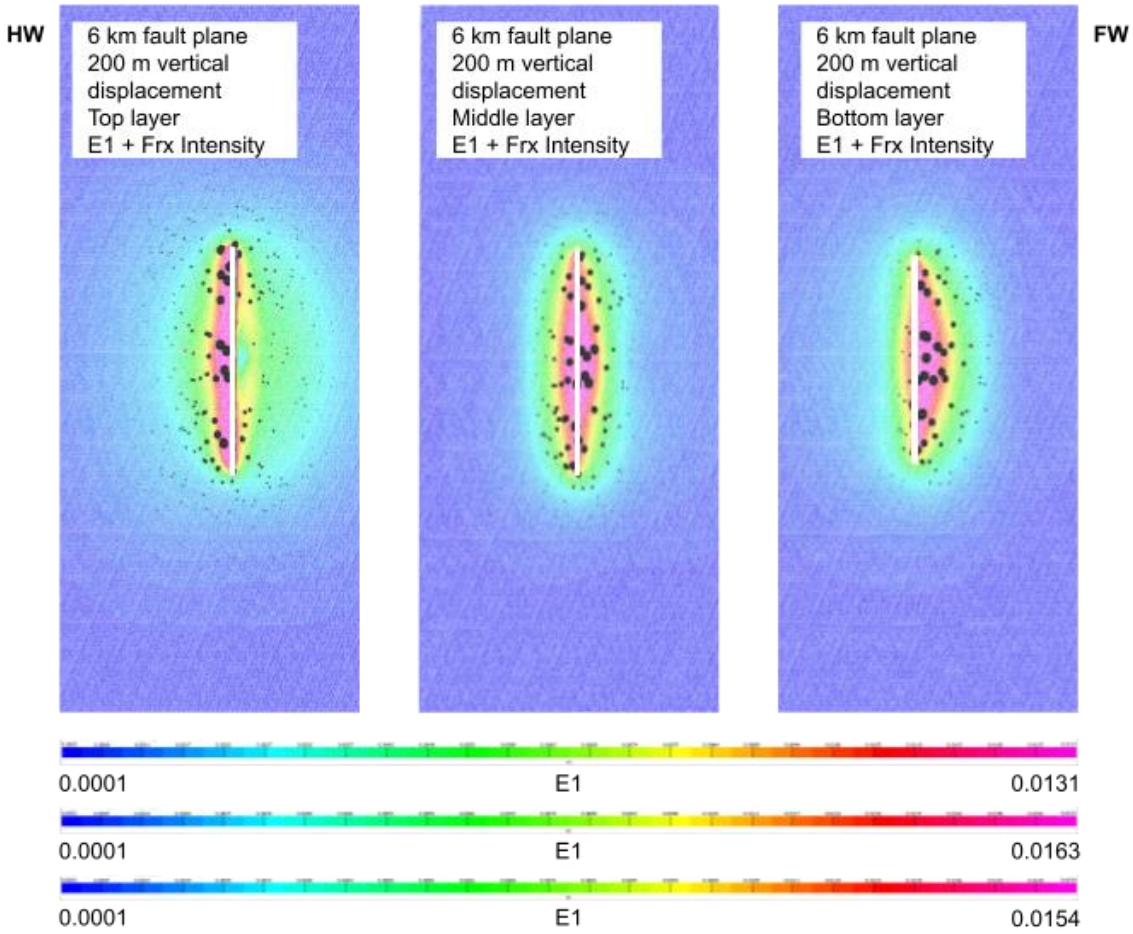

Figure 16. Damage zone distribution with depth. Predicted E1 values and fracture intensities for the 0.5 km-depth surface (left), 2 km-depth surface (middle), and 3.5 km-depth surface (middle) of a 6 km fault plane experiencing 200 m of vertical displacement. These models represent 3 different depths of the CL End stage of the Constant Length growth model. Warmer colors represent higher values; cooler colors represent lower values. Fracture intensity is also depicted on the E1 surface, with larger black dots representing greater fracture intensity at a given point.

The numerical values of MCSS, E1, and dilation predicted by the models also change between observation surfaces; within the same model, the middle observation surface (2 km depth) predicts the highest values, with the bottom layer displaying slightly lower values, and the top observation surface demonstrating the lowest (Fig. 17). Since each observation surface in a model scenario undergoes the same vertical displacement, the origin of these differences between different depths likely originates from the influence of increasing overlying confining

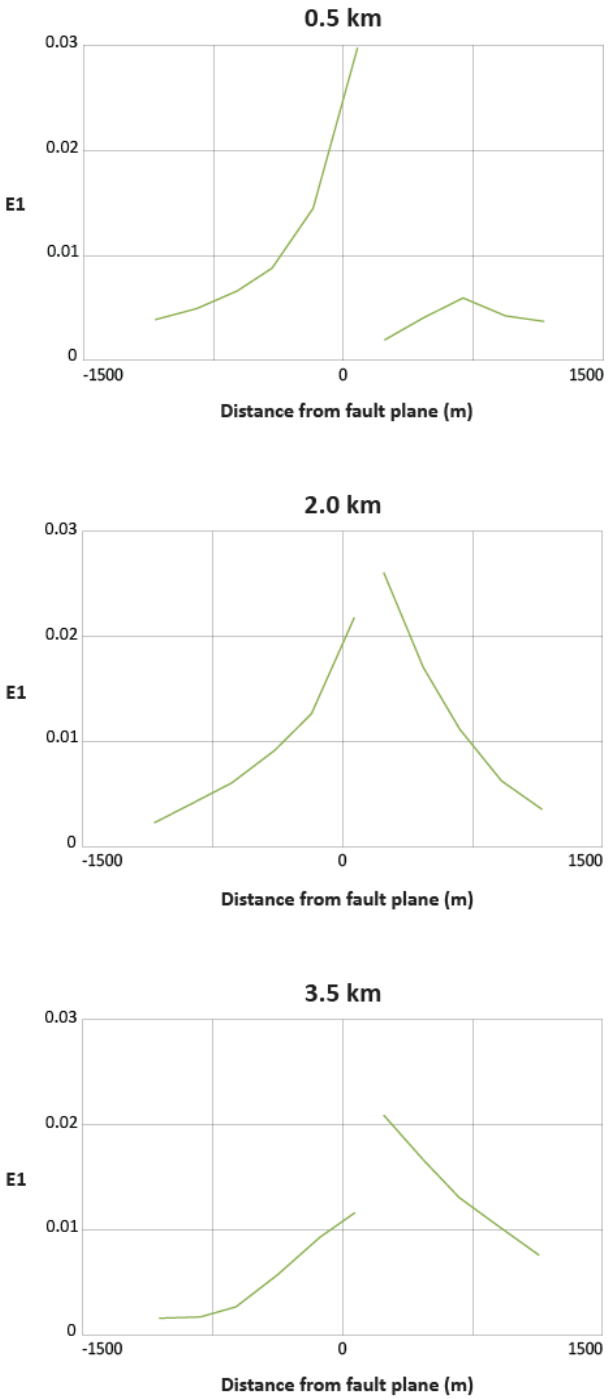

Figure 17. Graphical representations of E1 values at 0.5 km (top), 2.0 km (middle), and 3.5 km (bottom) depths around a 6 km fault plane experiencing 200 m of vertical displacement. These models represent 3 different depths of the CL End stage of the Constant Length growth model. As depth increases, elevated E1 values shift from the hanging wall side of the graph (0.5 km depth) to the footwall side of the graph (3.0 km depth).

pressure with depth. In deeper parts of the fault system, stress and strain in the rock body is being influenced by the movement of the fault and the pressure of the rock layers above it at the same time, generating distinct differences in these variables deeper into the subsurface. Greater confining pressures shift the Mohr circle right, such that failure is less likely to occur. Thus, damage zones at deeper depths within the fault system are responding to different confining pressures generated by overlying material and could be experiencing different patterns of failure which manifest in different parts of the fault zone. The elliptical model of fault slip distribution I used for modeling may also play a role in damage zone variation with depth. At greater depths, fault slip is distributed across a shorter horizontal distance around the fault center when compared to shallower depths in the model (Fig. 7). Thus, fault-slip tapering could also

control the location of damage zone development across a fault zone.

Fault Growth Models (FP vs. CL)

For the different fault propagation models, the relative location of MCSS, E1, and dilation maximums and minimums for each observation surface remains consistent, with the highest values observed near the fault center, and decreasing values associated with the fault tips. However, this pattern is shortened proportionally to the fault plane in the start and middle stages of the FP model. For example, we can observe that the same general spatial pattern of damage zone development exists between fault propagation models, but that the extent of a predicted damage zone is related to the fault's length (Fig. 18). However, the lateral extent of the predicted

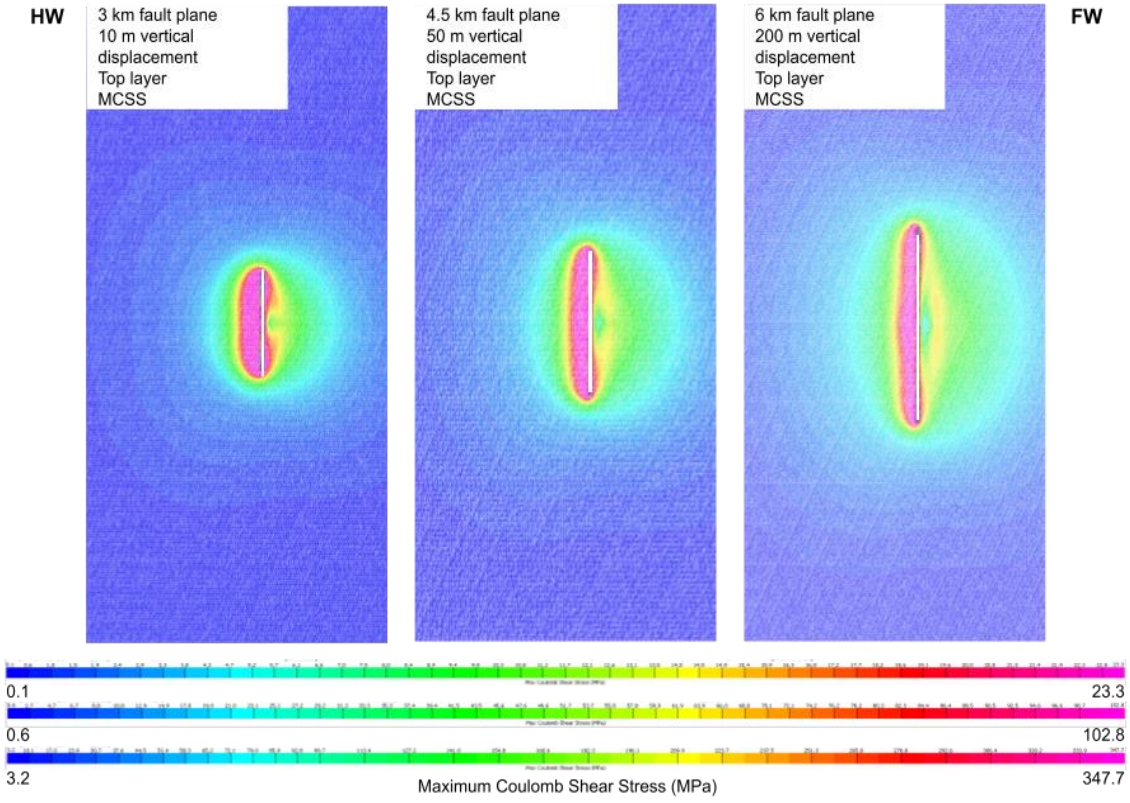

Figure 18. **Fault propagation (FP) model of fault growth**. Predicted MCSS for the 0.5 km depth surface of a 3 km fault plane experiencing 10 m of vertical displacement, representing the FP start model (left); a 4.5 km fault plane experiencing 50 m of vertical displacement, representing the FP Mid model (middle); and a 6 km fault plane experiencing 200 m of vertical displacement, representing the FP End stage of the Fault Propagation model of fault growth. Models include realistic pore fluid pressures. Warmer colors represent higher values; cooler colors represent lower values.

damage zones in the x direction (perpendicular to the fault plane) remains consistent between different stages of the fault propagation models (Fig. 19).

Numerically, the fault propagation models at every stage generate greater predicted E1, MCSS, and dilation values than for the constant length models experiencing the same vertical displacement, in the same material, and measured at the same depth.

For the starting phase of the fault propagation model, when the fault plane extends laterally for 3 km and the system undergoes 10 m of vertical displacement, we observe MCSS values between 4.8 MPa and 61.95 MPa; E1 values between 0.00021 and 0.0022; and dilation values between -0.00012 and -0.00082 across the top layer. For the starting phase of the constant length model, when the fault plane extends laterally for 6 km and the system undergoes 10 m of vertical displacement, we observe MCSS values between 4.24 MPa and 34.34 MPa, E1 values between 0.000216 and

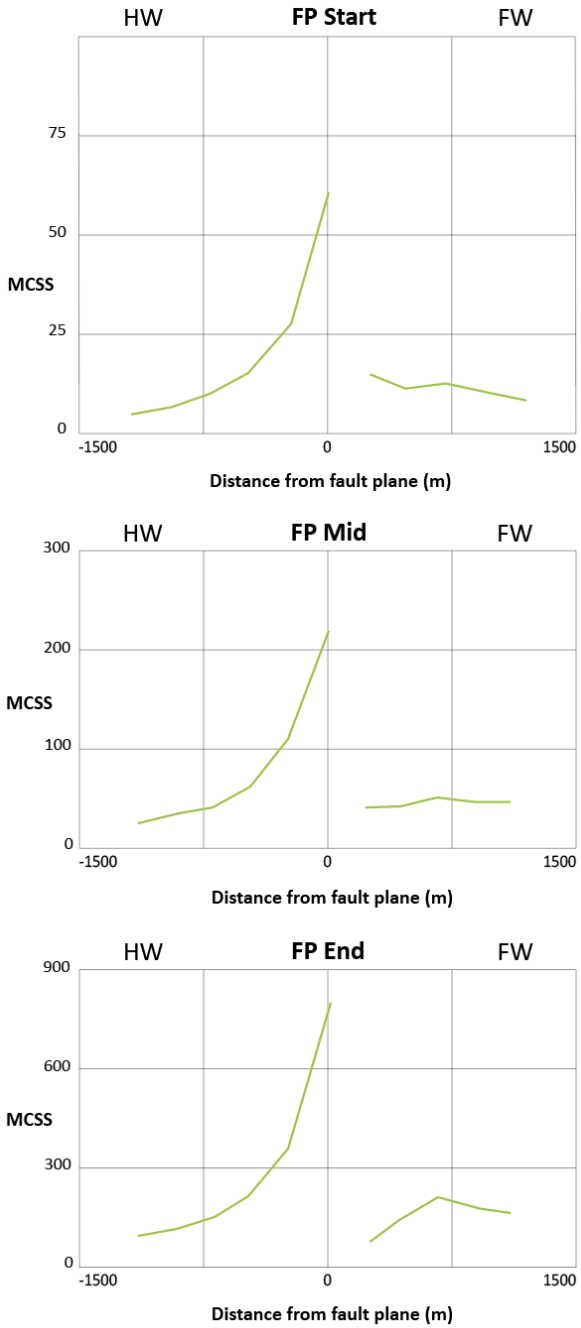

Figure 19. Graphical representations of MCSS values for the models in Figure 18. As fault propagation within the Fault Propagation conceptual model of fault growth continues, predicted MCSS values increase.

0.0012, and dilation values between -0.00013 and -0.00085 across the top layer. This difference in variable values can be seen clearly when graphed (Fig. 20).

Between FP and CL models experiencing the same amount of fault displacement, the fault plane is sized differently, with starting FP models only half as long as all CL models. Thus, although displacement remains the same in both models, the flexure is more concentrated in the FP start and mid models. This concentrated fault-related flexure would therefore distribute forces related to flexure over a smaller region resulting in greater stress and subsequent strain. Most likely, this fundamental relationship between flexure, fault plane area, stress, and strain is generating the distinctly larger MCSS, E1, and dilation values observed in FP models (i.e., same flexure of rock concentrated on fault planes with smaller areas, generating greater stress and strain values).

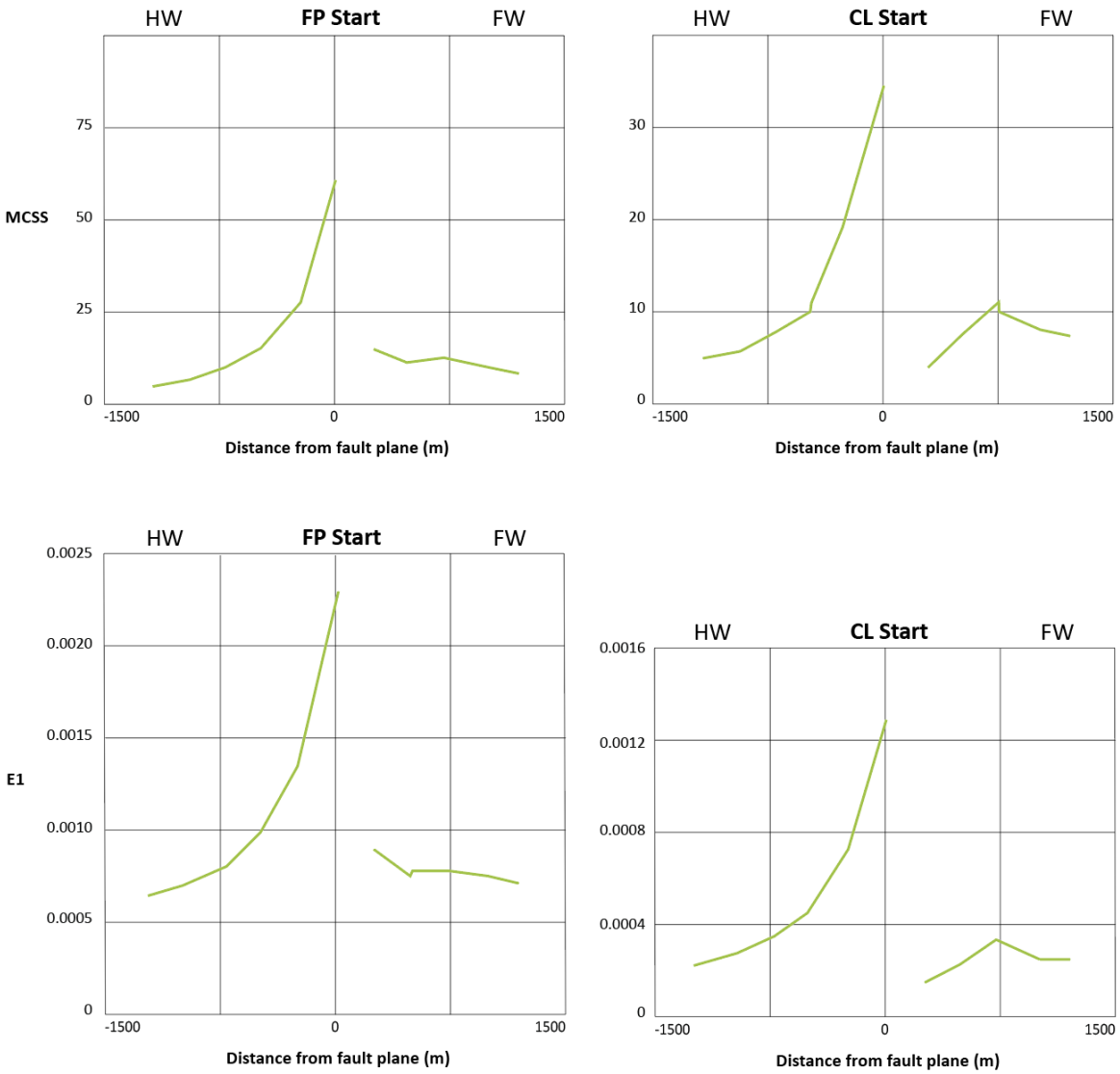

Figure 20. Graphical representations of maximum Coulomb shear stress (top) and E1 (bottom) predicted for a 3 km fault plane experiencing 10 m of vertical displacement, representing the FP Start stage of the Fault Propagation model (left) and a 6 km fault plane experiencing 10 m of vertical displacement, representing the CL Start stage of the Constant Length fault growth model. For the same stage (starting vs. ending) in the FP fault growth model (left) and the CL fault growth model (right), predicted MCSS and E1 values are higher in the FP models compared to the CL models.

Pore Fluid Pressure

The location and volumetric extent of damage zones between models with different pore fluid pressures remain consistent. However, the values predicted for MCSS, E1, and dilation vary with changes in PFP. Generally, in models with a set PFP value of 0 MPa for each observation surface, the MCSS recorded at a given point is lesser than for an equivalent model with a realistic pore fluid pressure. For example, the range of MCSS values predicted at the center of a fault plane in an end-stage CL model with realistic PFP is between 84.76 MPa and 804.95 MPa for the top layer; between 97.17 MPa and 694.74 MPa for the middle layer; and between 67.20 MPa and 584.17 MPa for the bottom layer. For an end-stage CL model with no PFP, this range shifts to between 89.03 MPa and 686.90 MPa for the top layer; between 96.42 MPa and 563.42 MPa for the middle layer; and between 67.20 MPa and 584.17 MPa for the bottom layer. A trend of lowered MCSS values in models with no pore fluid pressure is observed in the top and middle observation surface, but not in the bottom (3 km depth) layer, which shows the same range of values as the same model with realistic PFP (Fig. 21). In contrast, E1 and dilation values stay consistent between models with a PFP of 0 MPa and models with realistic PFP values. Through comparisons of the MCSS, E1, and dilation graphs for the top layer of the no-PFP model and the realistic-PFP model, we can see that the E1 and dilation values at a given point match exactly between models, while the MCSS varies.

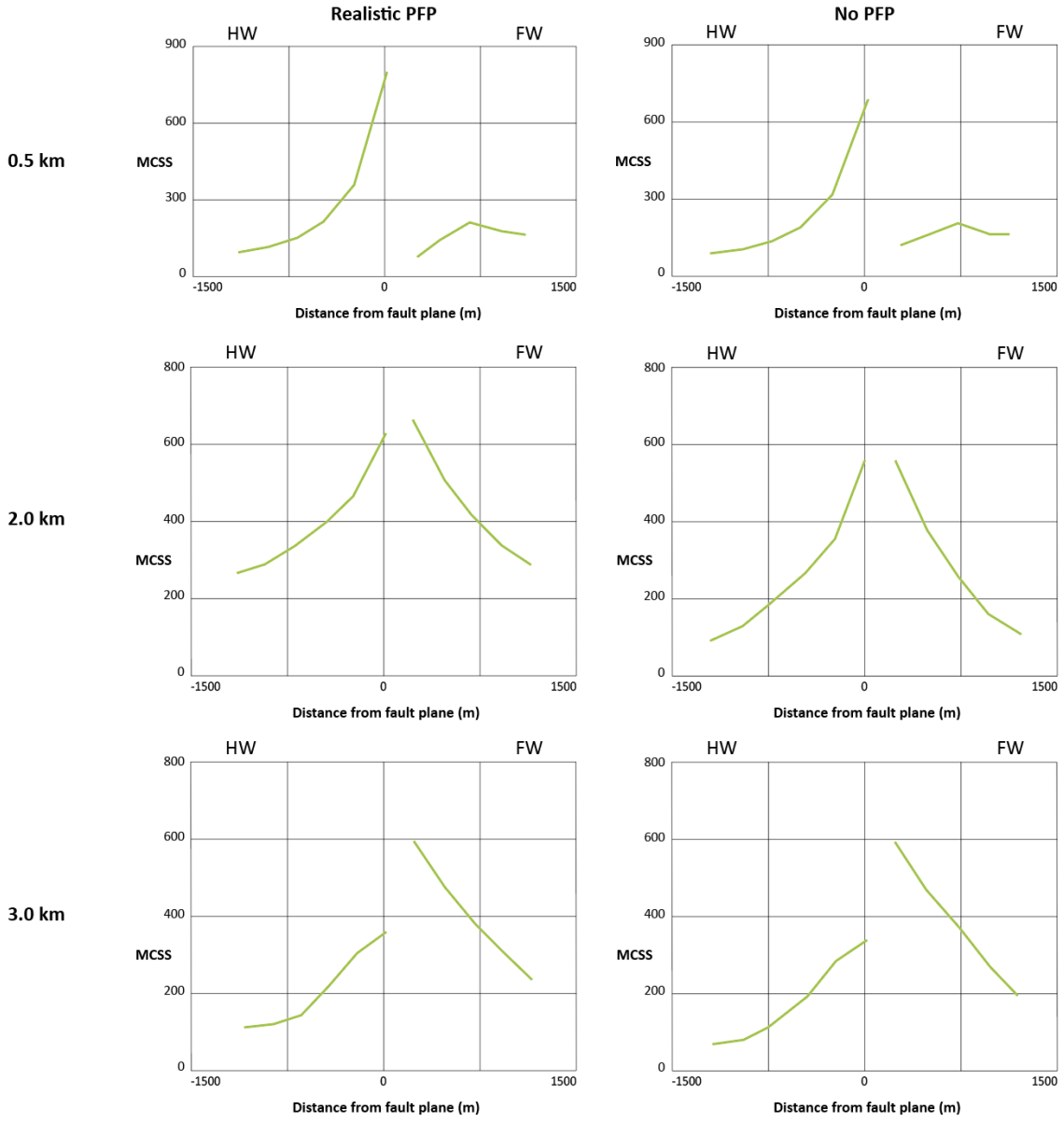

Figure 21. Graphical representations of MCSS (in MPa) for 0.5 km, 2 km, and 3.5 km-depths for a 6 km fault plane experiencing 200 m of vertical displacement. Graphs on the left are for models with realistic pore fluid pressures; graphs on the right are for models with pore fluid pressure values of 0. In models with no pore fluid pressure AND models with realistic pore fluid pressures, elevated MCSS values shift from the hanging wall at near-surface (0.5 km) depths to the footwall and greater 3.0 km depths. For the 0.5 km and 2.0 km surface depths, models with pore fluid pressure predict higher MCSS values; at 3.0 km depth, models with no PFP and realistic PFP values predict the same MCSS values.

DISCUSSION

Our modeling results predict a few key trends in damage zone development within normal fault zones. In summary:

1. The most intense damage zones across a fault are observed in the central portion of the fault plane, rather than at the tips;

2. Damage zone widths remain relatively constant as vertical displacement accumulates, even as stress and strain values increase with slip;

3. Damage zones may develop asymmetrically across a fault plane above and below the locus of maximum slip on a fault plane - the damage zone is wider in the HW than the FW at near surface depths but wider in the FW than the HW at deeper observation surfaces;

4. Predicted fracture intensities are greatest in damage zones associated with the highest fault displacements;

5. Fractures tend to orient themselves towards the fault tips near the ends of the fault plane, but are parallel or subparallel to the fault plane in major damage zones near the center of the fault plane;

6. The distribution of damage zones around a fault plane remains consistent between models and individual stages of fault propagation, but stress and strain values predicted for a given vertical displacement are greater in early stages of the Fault Propagation (FP) model that for early stages of the Constant Length (CL) model of fault growth;

7. Locations of damage zones for models with different pore fluid pressures remain consistent, but stress and strain variables at most depths are greater in models with greater pore fluid pressure values.

Modeling results are a direct function of the parameters established by the modeler's specifications and the type of modeling used. As previously described, the Fault Response Modeling module of *Move 2022* (by Petex) utilizes boundary element modeling (BEM) to predict stress, strain, and deformation responses (e.g., fracture formation) caused by a user-defined faulting event. BEM relies on a numerical computing method that solves partial differential conditions using defined boundary conditions within a model (Nikolic et al., 2016).

In a geological model, this typically means calculating displacements and tractions (stresses acting on surfaces) along elements such that displacements and stresses can then be calculated at any established point within the model interior (Cooke, *unpub*.). BEM models permit the user to apply loading to disrupted systems (e.g., a rock body with a fault plane), helping to illustrate the resulting deformation. This modeling is most helpful for studies which simulate deformation related to faulting because only the discontinuous surface of the fault is discretized, promoting calculation efficiency while maintaining accuracy around the fault (Crider and Pollard, 1998; Cooke, *unpub*.).

The FRM module also approximates faulting by calculating values for variables of interest based on the movement of rock in the hanging wall and footwall relative to the fault plane; however, this module does not fully consider the influence of frictional sliding between the hanging wall and footwall along the fault plane. Though frictional sliding likely plays an important role in deformation, including helping to determine the location and intensity of damage zones (e.g., Savage and Cooke, 2010), the movement and flexure of material around the fault plane also plays a large role in controlling fault-related deformation. Our model closely approximates a “weak” normal fault zone, in which even small amounts of slip along the fault can lead to comminution (grain-size reduction), thus the decreasing impact of friction on damage zone development (e.g., Brodsky et al., 2011; Collettini et al., 2019).

In these weak fault zones, frictional resistance to the motion of the fault drops as damage increases and the fault core develops (e.g., Collettini et al., 2019), meaning that as fault displacement increases, the impact of friction along the fault core becomes less influential on the accumulation of further damage. Since my models ultimately undergo high levels of displacement (10, 50, and 200 m), the relative impact of friction on damage zone development,

after initially established, is likely low. However, frictional resistance does influence damage close to the fault plane, meaning that frictionless models cannot provide tight constraints upon the development of damage zone architecture (Fig. 4E). Instead, stress and strain values predicted in frictionless models indicate the *susceptibility* of a material to failure throughout the rock volume adjacent to a fault. Thus, my major conclusions still apply to real-world systems, with the understanding that frictional resistance will cause some variation between my model results and real-world damage zone development.

In some cases, BEM's focus on boundary conditions can also make it difficult to apply generated results to highly heterogeneous materials within a rock body. Because my models focus only upon the homogeneous Navajo Sandstone, boundary element modeling remains the best method for my purpose – elucidating the evolution of fault damage zones. However, the relatively simple nature of computer models means that generated results cannot automatically be applied to more complex real-world systems. Instead, placing model results in the context of field studies and other modeling experiments can demonstrate the validity of model results and highlight useful insights that the model results provide. One clear connection between my modeling results and prior field studies (e.g., Cowie and Shipton, 1998; Berg and Skar, 2005) is in the predicted distribution of damage zones around the fault plane. In my investigation, regions of high stress, strain, and intense fracturing are concentrated near the center of the fault plane, with less intense stress and strain values observed in rock volumes beyond the fault tips, consistent with these field studies (e.g., Fig. 12).

Damage Zone Distributions

Damage zones are typically analyzed based on their structural position within the fault system and thus are commonly classified as wall, tip, and linking damage zones (e.g., Kim et al.

2004). These different damage zones vary both in the type of deformation expected and in the relative intensity of stress and strain (e.g., Kim et al., 2004; Choi et al., 2016). Field studies of fault-related fracturing in the Navajo Sandstone, where it is displaced by the Sevier fault, revealed evidence of high-intensity fracturing along the fault plane, with the intensity of fracturing dying out with increasing lateral distance from the approximate location of the fault tip (Nishimoto, 2022; 2023).

However, other field studies and modeling tests demonstrate an increase in stress, strain, and/or brittle deformation at fault tips relative to the fault center (e.g. Crider and Pollard, 1998, Wibberley et al., 2008). The discrepancy between my results (which focus upon a single normal fault) and other studies (which commonly analyze multiple interacting segments in a real-world normal fault system) likely stem from the fact that multiple interacting fault segments can communicate stress between themselves and generate a region of especially high stress and strain between fault tips (e.g., Crider and Pollard 1998, Nicol 2016). My models represent a fault segment experiencing no interaction with other faults, negating the influence of fault linkage on predicted damage zone distributions. Therefore, the predicted emphasis on high stress and strain near the fault center may represent a realistic prediction for more isolated fault segments. It also reinforces that stress and strain values within damage zones vary with position along a fault segment. Although greater total displacement and associated strain in the adjacent rock volume may occur near the center of a fault plane, as a fault propagates laterally, stress and strain are amplified due to the deformation of new material occurring as the fault propagates into the unbroken rock volume (e.g., Kim et al. 2004). Thus, stress and strain do not decrease to zero at the tip lines of the fault plane.

Another key result from model results is that the greatest values of stress and strain occur immediately adjacent to the fault plane and decrease with distance (e.g., Fig. 15). This trend is well-documented in normal fault zone studies, with the frequency of fault-related deformation structures greatest near the fault core, and lower further out (e.g., Choi, 2016; Childs et al., 2009) (Fig. 4E). However, the width of elevated stress and strain regions adjacent to the fault plane are wider in this model-based investigation than those documented in similar displacement faults in the Navajo Sandstone. Berg and Skar (2005) documented fracturing along the Moab normal fault in southern Utah, establishing an asymmetric 210-m damage zone in the hanging wall and a 70-m damage zone in the footwall, associated with 950 m of vertical displacement along the fault plane. Although my model experiences less displacement (200 m maximum), regions of high stress and strain extend much further than 210 m into the hanging wall and 70 m into the footwall observed by Berg and Skar (2005). My graphs of stress and strain variables also demonstrate a gradual decrease towards 0 away from the fault zone, rather than the clear demarcation between fractured and intact rock necessary to establish a clear damage zone width (e.g., Fig. 19). Therefore, I suggest that the actual damage zone for each fault model is narrower than the area of elevated stress and strain values predicted around the modeled fault zone. It is likely that there are critical stress and resulting strain values at which fault damage might result in the intense fracturing of a damage zone as opposed to strain being accommodated by minor strain within the intact rock; however, I cannot quantify what those values might be based on model results.

In part because of this same issue, the precise relationship between vertical displacement and damage zone width is difficult to establish with these models. The FRM module does not account for pre-existing weaknesses when calculating stress and strain values, negating the

potential influence of early fracturing on further deformation. This relationship between pre-existing weaknesses, strain hardening, and later deformation is central to two models of damage zone evolution.

One model is best visualized using the criterion for frictional sliding (Fig. 22). In material that has already crossed the Mohr Coulomb Failure Envelope and experienced failure, further failure can either lead to damage in previously undeformed material OR sliding along established fractures. For either of these situations to occur, the Mohr circle for previously deformed material must intersect the criterion for frictional sliding due to a change in stress or conditions (Fig. 22). Within fault damage zones, if the Mohr circle intersects the frictional sliding envelope, further deformation within already-deformed damage zone material would indicate that damage zone width will not increase with increasing displacement. This theory relies on the idea that deformation can preferentially act on already weakened material, such that intact material around a fault plane remains intact and locations with fractures accumulate more and more deformation as displacement continues (e.g., Ferrill et al., 2001). In this way, damage zone width is fixed, and further displacement does not lead to significant widening.

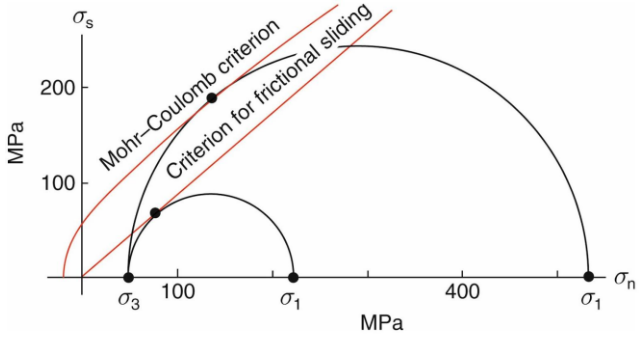

Figure 22. **Mohr-Coulomb criterion and criterion for frictional sliding**. Representation of the Mohr-Coulomb criterion for failure and criterion for frictional sliding. As differential stress (equal to stress1 – stress3) increases, the Mohr circle may intersect the Mohr-Coulomb failure criterion, meaning failure has occurred. If differential stress in this failed material later intersects the frictional sliding criterion, sliding may occur along pre-established fractures (modified from Fossen et al., 2016).

However, Berg and Skar (2005) suggest that strain hardening may occur within fault damage zones, such that deformed material becomes stronger compared to undeformed material

further from the fault zone. This hardening means that the frictional sliding criterion cannot be applied to deformed material, because it is now made stronger than nearby undeformed material, in fact widening the Mohr-Coulomb failure envelope (Fig. 9), perhaps requiring even greater differential stresses to form new fractures. In this strain-hardening model, undeformed material further from the fault fails as stresses generated by accumulating displacement along the fault plane propagate into the fault blocks. In this model, fault damage zones must widen with increased fault displacement (e.g. Knott, 1996; Cowie and Shipton, 1998; Berg and Skar, 2005).

Houwers et al. (2015) compiled field studies on damage zone widths across a variety of normal fault zones, using width and displacement relationships to establish a predictive equation for damage zone width at a given amount of vertical displacement. For each study, Houwers et al. (2015) determined that these variables best followed power law equations dependent on the faulted lithologies (Fig. 23). Cowie and Shipton (2005) studied faulting in the Navajo Sandstone. Other researchers documented fault zone deformation in different materials; for example, the Childs (2007) study took place in a more clay rich material (20% clay). Thus, equations from studies other than Berg and Skar (2005) and Cowie and Shipton (1998) are less applicable to my modeling but still illustrate the relationship between damage zone width and fault displacement. Notably, more clay-rich materials (relative to the clay-poor Navajo sandstone) display narrower damage zones in field studies, due to their weaker lithology; this is similar to the concept of pre-existing weaknesses in a rock limiting the rate of fault damage zone expansion with increasing fault displacement.

As a point of comparison, I plotted the fault displacement values and calculated damage zone widths from the Berg and Skar (2005) investigation, which was also conducted in the Navajo Sandstone. The Cowie and Shipton (1998) data predicted a fault displacement/damage

zone width relationship such that the damage zone width would equal 12.079 x (displacement)$^{0.5084}$ (Cowie and Shipton, 1998). Though data from the Berg and Skar (2005) paper is consistent with the Cowie and Shipton (1998) power law equation (Fig. 23), meaning this power law equation may be applicable across other faults in the same material.

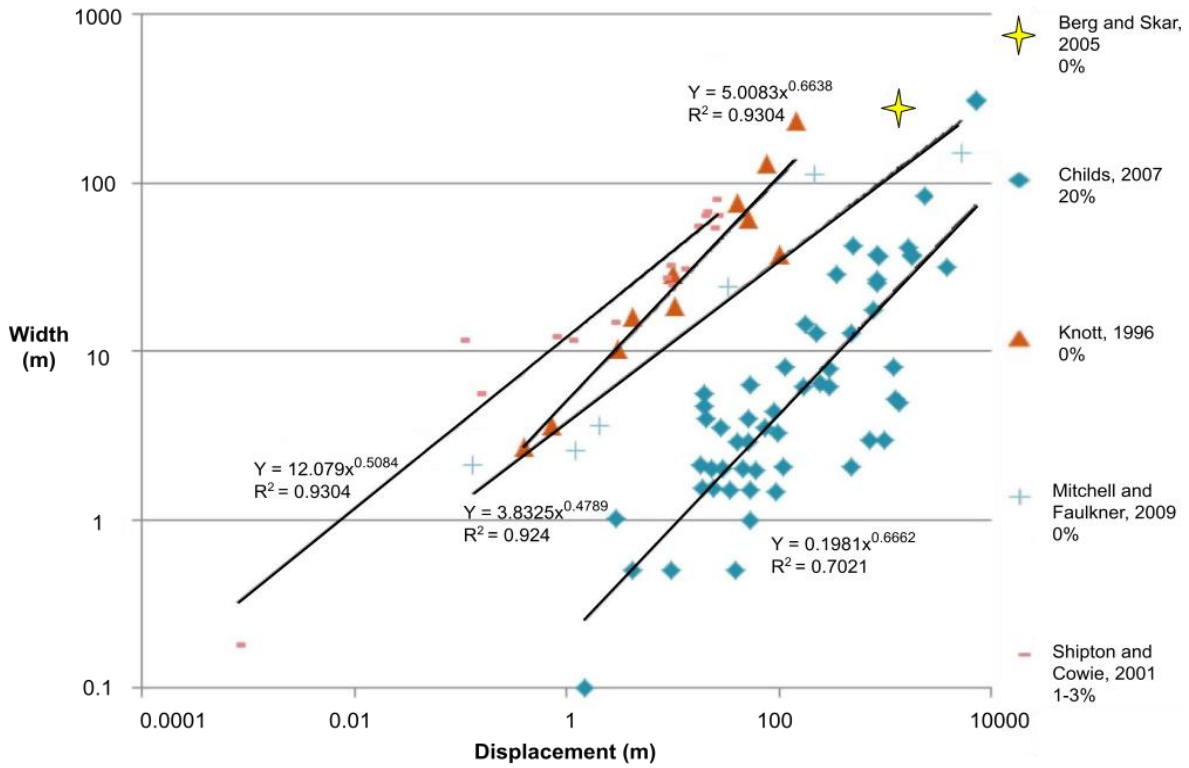

Figure 23. **Past studies of fault displacement vs. damage zone width**. Power law equations representing the relationship between damage zone widths and fault displacements calculated from various field studies (Childs, 2007; Knott, 1996; Mitchell and Faulkner, 2009; Shipton and Cowie, 2001). % in legend corresponds to % clay in involved units. A point representing the relationship between damage zone width and displacement found by Berg and Skar (2005) is also included. Modified from Houwers et al. (2015).

The power-law relationship indicates that although damage zone width increases with increasing fault displacement, the rate of damage zone widening decreases with increasing displacement. My models predict increasing stress and strain values with greater vertical displacement, with higher stress and strain values predicted at the same point in a higher-displacement model when compared to a lower displacement model. Although this seems to indicate that my models also predict an increase in damage zone width with increase in fault

displacement, the user cannot take pre-existing fracturing proximal to the fault plane into account in FRM modeling, so I do not consider this to be a true test of this hypothesis (increasing fault damage zone with increasing displacement).

Furthermore, friction at the fault plane is not considered when predicting damage zone widths in my models. Rather, stress and strain values are calculated based on flexure of material as the hanging wall moves down and the footwall moves upwards with displacement tapering away from the centroid (max. displacement location) on the fault plane. The presence of wide damage zones in our model results, based solely on flexure stresses, indicates that the flexure of material around the fault plane can widen damage zones in nature relative to what their width would be based on frictional stresses alone. Also, these flexure stresses set the stage for existing fractures to be acted on further by frictional forces, further developing damage zones. Thus, we would expect to see increasing damage zone widths with increasing vertical displacement along a fault due to increasing flexure and thus greater flexure stresses generated as faults accumulate displacement. Though more robust modeling that includes both frictional stresses *and* flexure will be needed to understand the exact relationship between vertical displacement and damage zone widths, these models provide an important demonstration of the forces that can influence this relationship.

Within my models, the higher predicted stress and strain values present further away from the fault plane in the hanging wall of the 0.5 km observation surface, relative to the footwall, suggests damage zone asymmetry. Such asymmetry has been documented in a field study of the same lithology (Navajo Sandstone), with a narrower damage zone in the footwall (70 m) of the normal fault versus the hanging wall (210 m) (Berg and Skar, 2005). Liao et al. (2020) demonstrate similar asymmetry in their interpretation of seismic data. Liao et al. (2020)

suggest that this asymmetry may be linked to an uneven distribution of stress created by the establishment of the hanging wall during fault propagation. Due to the relationship between stress and strain, unequal stress values across the fault plane must translate into uneven distributions of damage between the hanging wall and footwall (Berg and Skar 2005). Like both of these systems, my 0.5 km-depth models show wider damage zones in the hanging wall relative to the footwall.

Change in Damage Zone Distributions with Depth

This asymmetry holds true for all models at near-surface depths (0.5 km). However, at greater depths within a given model, damage zone asymmetry shifts such that all 3 km depth models show regions of high stress and strain values focused on the footwall rather than the hanging wall. I have not found previous studies that provide a satisfying answer to that explains this switch in damage zone location with depth. Since depth seems to be the controlling factor in changing asymmetries, such a shift may be due to increasing confining pressure changing the conditions for failure with depth. However, it is more likely that fault slip tapering and related fault propagation direction may play a more important role.

As described earlier, displacement gradients along a fault plane can be visualized as an ellipse with the greatest displacement at the center of the ellipse (centroid) and decreasing displacement that reaches 0 m at the fault tips (Fig. 7). This elliptical expression of displacement means that the actual displacement experienced by the rock volume is different at different depths along the fault plane at any given time. Because displacement accumulates, the fault plane above the centroid represents an area on the fault plane that experiences upward propagation of accumulating displacement, and the fault plane below the centroid represents an area that experiences downward propagation of displacement. Because the fault dips at an angle and

strain-related fracturing propagates in an orientation that is more energetically favorable, especially based on propagation direction (e.g., Sharon and Fineberg, 1996; Zhou et al., 2018; Fineberg and Bouchbinder, 2015; Surpless and McKeighan, 2022), this asymmetry is best explained by propagation direction as opposed to changing confining pressure, which should not change across a fault plane at the same depth beneath the surface.

Fracturing Intensity and Orientation

Understanding fracture intensity and orientation predictions is especially important for assessment of geothermal potential because increases in permeability created by fracturing and dilation create the primary pathways for circulating geothermal fluids in fault systems. My modeling results indicate that fracture intensities are greatest in regions of elevated stress and strain, meaning that the locations of high intensity fracturing in each model are subject to the same trends observed in damage zone locations. Fracture orientation, on the other hand, is not as easy to predict from stress and strain distributions. Instead, the orientation of a fracture at a given point is related to its position relative to the fault plane.

Near the fault tips of my models, fractures are oriented so that they point towards the ends of the fault plane. McGrath and Davidson (1995) observed relatively similar tip-related fracture orientations adjacent to normal faults of the Bristol Channel Basin. Closer to the fault center of my models, fracture orientations vary between the football and hanging wall. In the elongated damage zone of the hanging wall, fractures tend to form parallel or subparallel to the strike of the fault plane. In the footwall, fractures tend to form in orientations nearly perpendicular to the fault plane. Field studies of fracturing in normal faults also demonstrate orientation asymmetry between the footwall and the hanging wall, though the specific

orientations are different that those suggested in my models (e.g., McGrath and Davidson, 1995; Olson, 2004).

Typical field observations describe fractures forming parallel to the fault plane, like my models, but the hanging wall fractures form around 30 degrees from the plane (e.g., Olson, 2004), rather than the perpendicular orientations in my models. The growth of new structures is often defined by the dominant structure in a region, suggesting that the orientation of the fault plane dictates the geometry of new fractures in major damage zones. Because modeling in the FRM module cannot mimic frictional forces acting along the fault plane, we might expect not to see a difference in fracture orientation between the hanging wall and footwall, since friction helps drive fracture orientations towards perpendicularity with the fault plane. However, our models still demonstrate perpendicular fracturing in the footwall at near-surface depths, indicating that stress and strain from flexure with fault movement is sufficient to begin establishing different fracture orientations within damage zones, which may affect fracture orientations associated with frictional sliding along the fault plane. Thus, although the influence of the fault itself on fracture orientations cannot be included within my models, flexure-related stresses appear to play an important role in establishing the non-fault-parallel fracture orientations that have been observed in field studies (e.g., Olson, 2004).

I suggest that locations where fractures form parallel to the fault plane in our models would be the locations of greatest fracturing and therefore greatest permeability. I suggest this because if the locations where models predict fault-parallel fracturing related to flexure-related strain in the rock itself coincide with the predicted orientations of fault-related fractures formed due to shear stress acting between the hanging wall and the footwall (e.g., Olson, 2004), conditions for fracture orientations parallel to the fault plane are at their maximum. Thus, I

suggest that fault-parallel fracturing would be more intense and extend further into the fault block where both predicted model and theoretical fracture orientations match. This is an important relationship for geothermal energy development because fault-parallel fracturing produces the greatest connectivity of pore space, increasing permeability in a critical manner (e.g., Olson, 2004; Sharmin et al., 2023; Shervais et al., 2024).

Fault Growth Models: Fault Propagation vs. Constant Length

By comparing the damage zone extents between my Fault Propagation and Constant Length models, we can see that damage zones tend to follow the same distribution of high stress and strain around the fault plane, regardless of fault propagation model or stage. However, the sizes of these damage zones do vary with fault propagation model stage such that short fault planes in map view (the 3 km fault plane of FP start models and the 4.5 km fault plane of FP mid models) generated proportionally shorter damage zones in the fault-parallel direction. Still, both the FP model set and the CL model set concluded with a 6 km fault plane experiencing 200 m of vertical depth, and the associated stress and strain variable predictions for these final stages of each fault propagation model set produced essentially identical damage zone distributions. Such a discrepancy in damage zone area between early-stage FP and CL models indicates that, prior to accumulating large amounts of vertical displacement and/or reaching a final lateral length, damage zones would form differently based on the relationship between fault propagation and displacement accumulation. However, once a fault has neared its final lateral length and vertical displacement, the size and distribution of associated damage zones would likely not reflect fault propagation history. The fault propagation model and constant length model produce the same predicted stress and strain distributions when applied to a fault plane with the same accumulated vertical displacement and length.

Influence of Pore Fluid Pressure

My models also indicate that systems with realistic pore fluid pressures (PFPs) record higher MCSS and E1 values than systems with PFP values of 0. This is true of the top and middle layers of all models, though the bottom layer variable remains similar between realistic PFPs and PFPs of 0. When considering the Mohr Coulomb failure envelope, failure in material occurs if the shear and normal stress values are such that the Mohr circle intersects the failure envelope (Fig. 9). Higher pore fluid pressure shifts the Mohr circle towards the left, meaning that failure is far more likely to occur (Fig. 24). The elevated strain values observed in models with

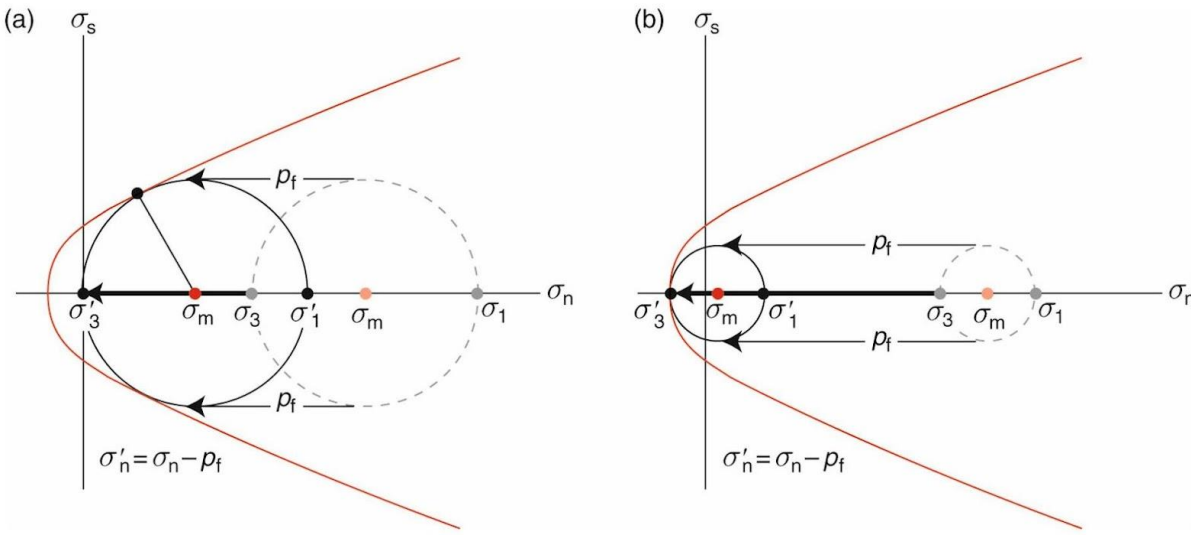

Figure 24. **Impact of PFP on Mohr circle**. Effect of increased pore fluid pressure on Mohr circle diagram. Increasing pore fluid pressure shifts the Mohr circle leftwards, changing the conditions for failure and allowing failure to occur at lower differential stress values. The leftwards shift due to increased pore fluid pressure can also change the type of fracturing occurring. Model A has not crossed the shear stress axis, indicating shear opening. However, increased pore fluid pressure in model B shifts the Mohr circle across the shear stress axis, indicating tensile opening. Modified from Fossen (2016).

realistic PFP values, relative to in models with no PFP, thus likely reflect the leftwards shift towards failure. Notably, the bottom layer of each model predicts the same MCSS and E1 values regardless of whether the model included realistic PFP values or PFP values of 0. Due to the elliptical shape of fault slip distribution utilized in my models, slip occurs over a very small

length along the fault plane, potentially reducing the impact of other variables (like PFP) on stress and strain. Still, the reasons for the discrepancy in PFP-stress-strain relationships at the lowest depths of the fault model are ambiguous but may be related to the increase in lithostatic load with increase in depth at a higher rate (rock density is greater than water density) so that PFP values at greater depths will have less of an impact relative to the higher lithostatic loads.

Implications for Geothermal Energy

Based on my model results and published field studies, the location and nature of damage zone development around a normal fault system can vary, depending on factors like 1) amount of vertical displacement experienced by the fault, 2) stage of fault propagation; 3) pore fluid pressure; and 4) depth (in relation to the slip-tapering centroid). Furthermore, damage zones tend to form asymmetrically near the map-view center of normal fault planes, with these changes likely associated with upward vs. downward-propagating faults. Damage zones may be established early in the history of a normal fault, with further stresses acting on pre-existing fracture networks before breaking intact rock outside the existing damage zone (e.g., Ferrill et al. 2001), but it is also possible that damage zone width will increase with increasing displacement (e.g., Berg and Skar, 2005; Houwers et al., 2015). The high fracture intensities and dilation values (and thus likely high permeability) observed in the damage zones of my models provide insights into damage zone development that can be used to better understand geothermal energy potential in normal fault zones and for constraining potential targets for future field-based geothermal exploration.

In its most recent geothermal report, the DOE predicted that the resources needed to produce 30,000 MWe (million watts of electricity capacity) are currently housed in "undiscovered" hydrothermal systems across the world, with enough to generate 26,000 MWe in

the contiguous United States (U.S. Department of Energy, 2019). However, while most currently tapped geothermal resources come from "identified" sources that show some evidence of hydrothermal activity at the Earth's surface (i.e. fumaroles, etc.), "undiscovered" systems typically require crustal penetration to be identified, explored, and then judged for geothermal energy suitability. This represents a significant up-front cost to potential geothermal investors (in both the corporate and governmental sectors), and ultimately forms one of the most prominent barriers to geothermal energy development in the United States (e.g., Micale et al., 2014; U.S. Department of Energy, 2019).

Given that geothermal energy is one of the most promising renewable energy resources of the 21st century, with the potential to generate 2-4 times as much electricity as wind or solar energy at the same installed capacity (Fig. 25), finding ways to minimize the cost of geothermal exploration will be crucial for promoting green energy and developing resilient electricity through resource diversification (U.S. Department of Energy, 2019). 3D modeling, which can be done in advance of expensive field studies, represents a potential method for better identifying damage zones that can support utility-scale geothermal energy production. Modeling may not perfectly image a real-world fault zone, but it can illuminate trends in stress and strain

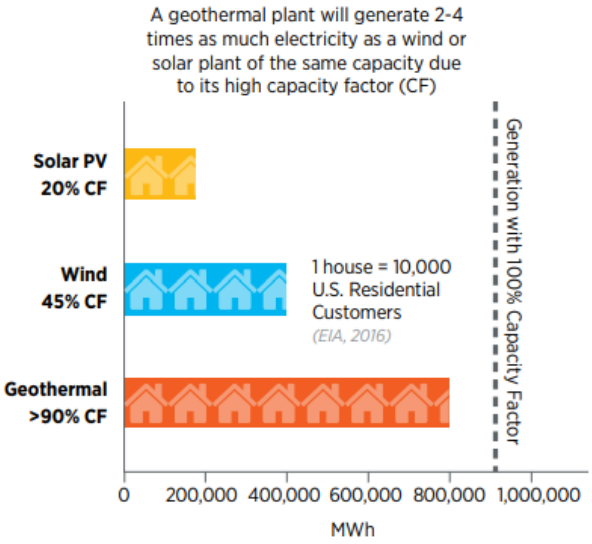

Figure 25. Comparison of calculated capacity factors (CF) for 3 common sources of renewable energy: Solar (yellow), Wind (blue), and Geothermal (orange) (U.S. Department of Energy, 2019).

that help create an understanding of where geothermally promising permeability exists in different geological settings and depths.

My models suggest that geothermal development up to 1 kilometer of depth may be successfully targeted to locations in the hanging wall near the fault. Furthermore, they also suggest that regions with elevated pore fluid pressure likely demonstrate more developed damage zones relative to regions with no or low values of pore fluid pressure. These results, along with the many other predictions 3D modeling software can generate, demonstrate that modeling can help researchers better understand stress, strain, and damage across fault zones, helping to better inform where to target traditional methods of geothermal exploration (such as drilling sample wells). Thus, further developing 3D modeling techniques while also further investigating damage zone development processes in normal fault systems will continue to be vital in a global shift towards geothermal energy expansion.

CONCLUSION

By modeling normal fault zones to constrain the impacts of different amounts of fault displacement, different conceptual models of fault growth, and different pore fluid pressure values across multiple depths, I have illuminated key trends in damage zone development. These include:

1. High-intensity damage zones (with high-intensity fracturing) form near the center of a fault plane, while stress and strain values decrease closer to the fault tips. This trend holds true for all modeled scenarios, and predicted stress and strain values in these damage zones increase with greater fault displacement.

2. Damage zones commonly form asymmetrically across the fault plane; however, the direction of asymmetry varies with depth. At near-surface depths, where upward propagation of displacement is most likely, the hanging wall experiences a wider damage zone relative to the footwall. At greater depths, where downward propagation may occur, the footwall experiences a wider damage zone relative to the hanging wall.
3. Damage zone distribution around the fault plane is consistent for every stage of the Fault Propagation and Constant Length models, such that regions with the greatest predicted damage occur near the fault plane center. However, stress and strain values are greater in early stages of the Fault Propagation model relative to Constant Length models experiencing the same amount of vertical displacement.
4. Locations of damage zones between models with different pore fluid pressures remain consistent, but stress and strain values at most depths are greater in models with greater pore fluid pressure values.

Due to the strong relationship between fault-related damage zone development and elevated subsurface permeability, these identified trends in damage zone formation can provide insight into where geothermal energy systems can best be targeted. My results suggest that a fault's propagation history, damage zone asymmetry between the hanging wall and footwall, the depth of resources to be targeted, and pore fluid pressures all exert controls on possible fluid flow rates and flow paths, which are important for geothermal implementation in a normal fault zone environment. These results represent a useful framework for targeting geothermal potential in normal fault zones and emphasize the utility of 3D modeling for geothermal exploration.

REFERENCES

Andrews, J., and Jelley, N., 2022, Energy Science: Principles, Technologies, and Impacts: Oxford, U.K., Oxford University Press, 512 p.

Berg, S.S., and Skar, T., 2005, Controls on damage zone asymmetry of a normal fault zone: outcrop analyses of a segment of the Moab fault, SE Utah: Journal of Structural Geology, v. 27, p. 803-1822.

Blackwell, D., Richards, M., Frone, Z., Batir, J., Ruzo, A., Dingwall, R., and Williams, M., 2011, Temperature at depth maps for the conterminous US and geothermal resource estimates, GRC Transactions, v. 35.

Boden, D.R., 2017, Geologic Fundamentals of Geothermal Energy: Boca Raton, Florida, CRC Press, 399 p.

Brodsky, E.E., Gilchrist, J.J., Sagy, A., and Collettini, C., 2011, Faults smooth gradually as a function of slip, Earth and Planetary Science Letters, v. 302, p. 185 – 193.

Cartwright, J.A., Mansfield, C., and Trudgill, B., 1996, The growth of normal faults by segment linkage, Geological Society Special Publications, v. 99, p. 163 – 177.

Chelminksi, K., 2022, Climate Finance Effectiveness: A Comparative Analysis of Geothermal Development in Indonesia and the Philippines: Journal of Environment & Development, v. 31.

Childs, C., Manzocchi, T., Walsh, J.J., Bonson, C.G., Nicol, A., Schoepfer, M.P.J., 2009, A geometric model of fault zone and fault rock thickness variations, Journal of Structural Geology, v. 31, p. 117 - 127.

Choi, J.H., Edwards, P., Ko K., and Kim, Y.S., 2016, Definition and classification of fault damage zones: A review and a new methodological approach: Earth-Science Reviews, v. 152, p. 70 – 87.

Collettini, C., Tesei, T., Scuderi, M.M., Carpenter, B.M., and Viti, C., 2019, Beyond Byerlee friction, weak faults and implications for slip behavior, Earth and Planetary Science Letters, v. 519, p. 245 – 263.

Cooke, M., *unpublished*, Numerical Methods – Boundary Element Modeling, 3p.

Cowie, P.A., and Shipton, Z.K., 1998, Fault Tip Displacement Gradients and Process Zone Dimensions, Journal of Structural Geology, v. 20, p. 983 - 997.

Crider, J., and Pollard, D., 1998, Fault linkage: Three-dimensional mechanical interaction between echelon normal faults, Journal of Geophysical Research, v. 103, p. 24.373 - 24.391.

Cross, Jonathan, 2009, "2008 Geothermal Technologies Market Report": U.S. Department of Energy - Office of Scientific and Technical Information, United States, https://www.osti.gov/servlets/purl/1218467.

Faulds, J., and Hinz, N., 2015, Favorable Tectonic and Structural Settings of Geothermal Systems in the Great Basin Region, Western USA: Proxies for Discovering Blind Geothermal Systems, in Proceedings, World Geothermal Congress, Melbourne: Australia, Nevada Bureau of Mines and Geology (https://www.osti.gov/servlets/purl/1724082).

Ferrill, D.A., and Morris, A.P., 2001, Displacement gradient and deformation in normal fault systems, Journal of Structural Geology, v.23, p. 619 – 638.

Fineberg, J., and Bouchbinder, E., 2015, Recent developments in dynamic fracture: Some perspectives, International Journal of Fracture, v.196, 33 – 57.

Fossen, H., and Rotevatn, A., 2015, Fault linkage and relay structures in extensional settings- A review, Earth Science Reviews.

Fossen, H., 2016, Structural Geology: 2nd edition, Cambridge: Cambridge University Press.

Grant, M.A., and Bixley, P.F., 2011, Geothermal Reservoir Engineering: 2nd Edition, Cambridge: Academic Press.

Houwers, M.E., Heijnen, L.J., Becker, A., Rijkers, R., 2015, A Workflow for the Estimation of Fault Zone Permeability for Geothermal Production: A General Model Applied on the Roer Valley Graben in the Netherlands, in Proceedings, World Geothermal Congress, Melbourne: Australia.

Jackson, G.W., 1990, The Toroweap Fault: One of the Most Active Faults in Arizona, Arizona Geology, v. 20, p. 7 – 10.

Kim, Y.S., Peacock, D., Sanderson, D, 2004., Fault damage zones: Journal of Structural Geology v. 26. P. 503 - 517. DOI: 10.1016/j.jsg.2003.08.002.

Kim, Y.S., and Sanderson, D., 2005, The relationship between displacement and length of faults: A review, Earth Science Reviews, v. 68, p. 317 – 334.

Knott, S. D., Beach, A., Brockbank, P. J., Brown, J. L., McCallum, J. E., and Welbon, A. I., 1996, Spatial and mechanical controls on normal fault populations, Journal of Structural Geology, v. 18, p. 359 – 372.

Liao, Z., Hu, L., Huang, X., Carpenter, B.M., Marfurt, K.J., Vasileva, S., and Zhou, Y., 2020, Characterizing damage zones of normal faults using seismic variance in the Wangxuzhuang oilfield, China: Interpretations v. 8, p. 1- 24.

McGrath, A.G., and Davison, I., 1995, Damage zone geometry around fault tips, Journal of Structural Geology, v. 17, p. 1101 – 1024.

Micale, V., Oliver, P., and Messent, F., 2014, The Role of Public Finance in Deploying Geothermal: Background Paper, in San Giorgio Group Report, Climate Policy Initiative, p. 1 - 15.

Mitchell, T. M., and D. R. Faulkner, 2008, Experimental measurements of permeability evolution during triaxial compression of initially intact crystalline rocks and implications for fluid flow in fault zones, Journal of Geophysics Research, v. 113.

Nicol, A., Childs, C., Walsh, J.J., Manzocchi, T., Schopfer, M.P.J., 2017, Interactions and growth of faults in an outcrop-scale system, Geological Society of London Special Publications, v. 439, p. 23 – 39.

Nikolic, M., Roje-Bonacci, T., and Ibrahimbegovic, A., 2016, Overview of the Numerical Methods for the Modelling of Rock Mechanics Problems, Tehnicki Vjesnik, v. 23, p. 627 - 637.

Nishimoto, M., Surpless, B., and Monecke, K., 2022, Analyzing normal fault-tip damage zones: Geological Society of America Annual Meeting, Abstracts with Programs, Denver, CO.

Nishimoto, M., Surpless, B., and Monecke, K., 2023, Investigating normal fault damage zone development using virtual outcrop models: a case study of the Sevier normal fault, southern Utah: Geological Society of America, Southeastern/Northeastern Sections Joint Meeting, Abstracts with Programs, Reston, VA.

Olson, J.E., 2004, Predicting fracture swarms: the influence of subcritical crack growth and the crack-tip process zone on joint spacing in rock, Geological Society of London Special Publications, v. 231, p. 73 – 88.

Petex, 2020, Move 2020 Tutorial 33: Fault Response Modeling.

Rotevatn, A., Jackson, C.A.L., Tvedt, A.B.M, Bell, R.E., Blaekkan, I., 2019, How do normal faults grow? Journal of Structural Geology, v. 125, p. 174 – 184.

Savage, H.M., Brodsky, E.E., 2011, Collateral damage: Evolution with displacement of fracture distribution and secondary fault strands in fault damage zones, v. 116, p. 1 – 14.

Savage, H.M., and Cooke, M.L., 2010, Unlocking the effects of friction on fault damage zones, Journal of Structural Geology, v. 32, p. 1732 – 1741.

Schultz, R., 2010, Porosity and Grain Size Controls on Compaction Band Formation in Jurassic Navajo Sandstone: American Geological Union geophysical Research Letters v. 37, 22.

Sharon, E., Fineberg, E., 1996, Microbranching instability and the dynamic fracture of brittle materials: Physics Reviews, v. B54, p. 7128–7139.

Sharmin, T., Khan, N.Z., Akram, M.S., Ehsan, M.M., 2023, A State-of-the-Art Review on Geothermal Energy Extraction, Utilization, and Improvement Strategies: Conventional, Hybridized, and Enhanced Geothermal Systems, International Journal of Thermofluids, v. 18, p. 1 – 25.

Shervais, J. et al., 2024, Geothermal play fairway analysis, part 1: Example from the Snake River Plain, Idaho, v. 117, p. 1 – 18.

Speer, B., Economy, R., Lowder, T., Schwabe, P., Regenthal, S., 2014, Geothermal Exploration Policy Mechanisms: Lessons for the United States from International Applications: National Renewable Energy Laboratory, Technical Report, 64 p.

Surpless, B.E., and McKeighan, C., 2022, The role of dynamic fracture branching in the evolution of fracture networks: an outcrop study of the Jurassic Navajo Sandstone, southern Utah: Journal of Structural Geology, v. 161. DOI: 10.1016/j.jsg.2022.104664.

U.S. Department of Energy, 2019, Geovision: Harnessing the Heat Beneath our Feet: https://www.energy.gov/sites/prod/files/2019/06/f63/GeoVision-full-report-opt.pdf (accessed September 2023)

Walsh, J.J., Nicol, A., Childs, C., 2002. An alternative model for the growth of faults: Journal of Structural Geology, v. 24, 1669–1675.

Wibberley, C.A., Yielding, G., Di Toro, G., 2008, Recent advances in the understanding of fault zone internal structure: a review, Geological Society of London Special Publications, v. 299, p. 5 -33.

Zhou, S., Zhuang, X., Zhu, H., Rabczuk, T., 2018, Phase field modeling of crack propagation - Branching Coalescence Rocks: Theoretical Applications of Fracture Mechanics, v. 96, p. 174–192.